University of Alberta

Development of a Mid-infrared Detection System for Real-time Measurements of Gas Phase Benzene, Toluene, Ethylbenzene and Xylenes using a Tunable External Cavity Quantum Cascade Laser.

by

Boshra Momen Nejad

A thesis submitted to the Faculty of Graduate Studies and Research
in partial fulfillment of the requirements for the degree of

Master of Science

in

Photonics and Plasmas

Department of Electrical and Computer Engineering

Spring 2012
Edmonton, Alberta

To my beloved husband

and

my dear family

Abstract

The chemical transformation of trace gases, including reactions that result in aerosol particle formation, as well as the composition of the atmosphere deeply influence air quality and Earth's global climate. Use of a simulation chamber to study smog formation is a common method to investigate chemical transformations of trace gases. We focus our efforts on benzene, toluene, ethyl-benzene and m-, o-, and p-xylene gases (i.e., BTEX gases), which are often associated with air emissions from petroleum production industries. Studies have shown that these gases have multiple impacts on the environment and public health along with their effect on photochemical smog and ozone formation in the troposphere. We demonstrate our progress in developing an application of mid-IR continuous wave External Cavity Quantum Cascade Laser (EC-QCL) absorption spectroscopy for measurements of multiple trace gas species in combination with a smog simulation chamber. The results are compared to *in situ* measurements of the trace gas species with UV absorption spectroscopy.

Acknowledgements

I would like to express my honest appreciation to my M.Sc. Supervisors, Professor John Tulip and Professor Wolfgang Jaeger, for their support and encouragement.

I offer my special thanks to Dr. Matthew Parsons and Dr. Ihor Sydoryk for their generous support and help during my graduate studies.

I would also like to thank all of the Alberta Laboratory for Laser Spectroscopy and Atmospheric Sensing (ALLSAS) members, for their consideration and providing such a professional environment.

Last but not least, I would like to thank my beloved family for their love and support.

Table of Contents

List of Tables

List of Figures

Chapter 1

Introduction

1.1 Background

There is blanket of air surrounding Earth called atmosphere. The atmosphere is made of different layers. The layer in which we live and breathe is called troposphere. The troposphere, which contains approximately 80% of the mass of the atmosphere [1], extends up to 17 km [2] from the surface of Earth.

The atmosphere contains several gas phase and particle phase compounds. Nitrogen (78.08%), oxygen (20.95%) and argon (0.93%) are the major gases in the atmosphere [3]. There are other gases in the atmosphere which are mostly referred to as trace gases such as carbon dioxide, methane and ozone. The particle phase compounds found in the atmosphere include water vapor, dust, sea spray, volcanic ash and many other aerosol particles coming from natural and man-made sources. The main components of the unpolluted, dry atmosphere are shown in Table 1.1 [3].

Volatile organic compounds (VOCs) in the atmosphere are mainly emitted from forests and biomass burning. VOCs such as isoprene, α- and β-pinene and methanol are released by forests which are the largest sources for VOC emission [4]–[6]. VOCs emitted from biomass burning include oxygenated species (organic acids and carbonyls), nitriles (NH_3CN)and aromatics (benzene and toluene) [4], [7], [8].

Gas	Mixing Ratio Volume %
Nitrogen (N_2)	78.08
Oxygen (O_2)	20.95
Argon (Ar)	0.93
Carbon dioxide (CO_2)	0.037
Neon (Ne)	0.0018
Helium (He)	0.00052
Methane (CH_4)	0.00017
Krypton (Kr)	0.00011
Hydrogen (H_2)	0.00005
Dinitrogen oxide (N_2O)	0.00003
Xenon (Xe)	0.00009

TABLE 1.1
The main components of the unpolluted, dry atmosphere [3].

1.2 Motivation for Studying BTEX Compounds

Benzene, toluene, ethylbenzene, ortho-, and para-xylene (BTEX), which are mostly produced by petroleum industries [9], are mono-cyclic, aromatic hydrocarbons with molecular structures shown in Fig. 1.1 [10].

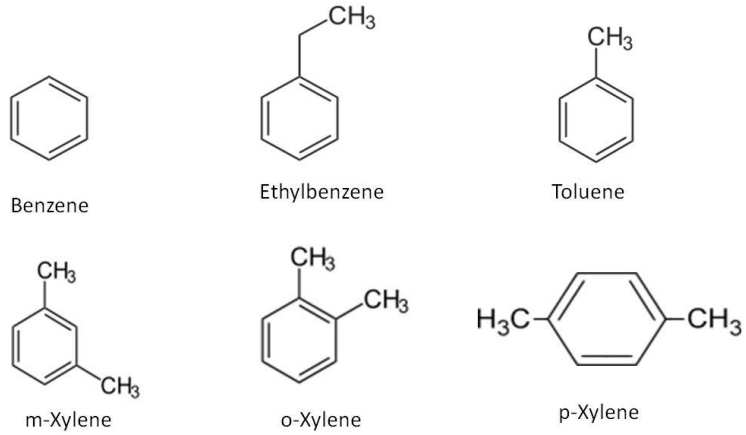

Fig. 1.1. Molecular structures of BTEX compounds [10].

According to the U.S. Environmental Protection Agency (U.S. EPA), BTEX compounds are toxic and carcinogenic and influence human health and Earth's environment [9]. As an example, the Occupational Safety and Health Administration (OSHA) has assigned exposure time limits to 1 *ppm* benzene, 200 *ppm* toluene and 100 *ppm* xylene of around 8 hours for industrial workers [11].

Health effects caused by BTEX compounds fall into two main categories: direct effects and indirect effects. Direct health effects of BTEX compounds are associated with being directly exposed to these compounds. For example, touching a liquid

containing BTEX compounds may cause skin irritation. These gases can also exist in the air you are breathing and cause respiratory problems [12].

These organic compounds also produce other air pollutants like aerosol particles by going through chemical reactions with hydroxyl radicals that are formed in the presence of UV radiation [13], [14] and in this way, they can indirectly affect human health. Aerosols are suspensions of liquid or solid particles in a gas and are of great importance for Earth's energy balance, climate change and human health [15].

The initiating reactions of aerosol formation simulated in a photoreaction chamber are shown in Eqs. 1.1 & 1.2. Aerosol particles are made by further reactions and condensation of the products [16].

$$H_2O_2 + h\nu(< 370nm) \rightarrow 2OH^{\bullet} \tag{1.1}$$

$$OH^{\bullet} + BTEX \rightarrow Products \tag{1.2}$$

The hydroxyl radicals, $OH^{\bullet}$, in atmosphere are produced from the reaction of excited atomic oxygen with water. They are also formed during UV-light dissociation of H_2O_2 [17], [18].

Aerosol particles can have negative effects on human health. The total health effects of these particles involve two main categories: direct health effects of aerosols and health effects as a result of climate change caused by aerosols [19].

When considering direct effects of aerosol particles on human health, their concentration, size, structure and chemical composition are important factors [15]. These particles may be toxic due to the presence of specific chemical or physical properties [20]. Aerosols may enhance cardiovascular problems, infectious and allergic diseases [15].

Particle size determines whether the aerosol particle would be deposited in the respiratory tract or not. Normally, particles with a diameter of more than 2.5 μm (coarse particles) will not get deep into the lungs [21]. On the other hand, particles with less than 2.5 μm diameter (fine particles) can go far deeper into the respiratory system and be deposited on the air exchange parts of the human lungs [22]. Ultrafine aerosol particles with less than 100 nm diameter, are of more concern as they

can damage the human central nervous system [19].

The climate and atmospheric effects of aerosol particles result from their ability to scatter and absorb solar radiation (cooling effect) and their role as condensation nucleus in the formation of clouds and rain [15]. Fig. 1.2 shows how aerosol particles cycle in the atmosphere [15].

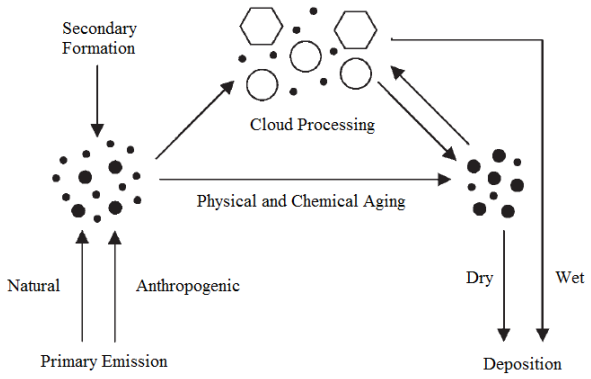

Fig. 1.2. Atmospheric cycling of aerosols in the atmosphere [15].

Aerosol particles have a total cooling effect on the global climate [19], and thus reduce the warming effect caused by greenhouse gases [19]. Besides, aerosols can affect cloud properties by increasing the droplet concentration and decreasing the droplet size [23], which may increase the reflection of solar radiation back into the space [19].

Aerosols can also cause poor air quality ("smog") which is a major concern in large cities. So real-time air quality monitoring would be another environmental approach of aerosol related studies [24].

The health effects of climate change are illustrated in Table 1.2 [19], [25].

1.3 Current Gas Sensing Technologies

Current technologies used for gas phase detection of BTEX compounds are included but not limited to the categories described in this section.

Some of the gas monitoring techniques take advantage of gas chromatography (GC) as their separation or selectivity step, in combination with a detector which can be a photo-ionization detector (PID), flame-ionization detector (FID) or mass spectrometer (MS) [11].

Environmental effect	Beneficial (+) and adverse (−) health effects	Aerosol effect
Warmer temperatures	+ Aero-allergen production: shorter pollen season in some regions + Crop increases in too-cold regions (at a limited warming) − Aero-allergen production: increased allergic disorders due to longer pollen season − Food-poisoning: increased risk at higher temperature (especially salmonellosis) − Water-borne infection: cholera risk might be amplified by water warming − Release of accumulated pollutants in some regions (e.g. mercury)	Totally cooling, but some aerosol components such as black carbon are heating atmosphere.
Temperature extremes	+ Reduced winter deaths in some countries − Increased mortality due to thermal stress	Reducing heat waves.
Floods	− Injuries/deaths − Infectious diseases − Mental health disorders − Exposure to toxic pollutants − Sewage and animal wastes into waterways and drinking water supplies	Increasing heavy rainfall, but decreasing floods caused by a warmer atmosphere. Influencing Himalayan glaciers.
Droughts	+ Water-borne infection: less risk where heavy rainfall diminishes − Crop reduction, especially in low-latitude regions	Unclear if aerosol decreases precipitation in some areas. Influencing Himalayan glaciers.
Ecosystem changes	+ Possibly more fish in some regions − Food poisoning, unsafe drinking water − Infectious diseases, e.g. malaria dengue, tick-borne viral disease − Decreased fish yields, impaired crops	A variety of effects depending on both climate change and toxicity of the partieles.
Sea-level rise	− Drinking water damages due to salivation of freshwater − Population displacement − Exposure to coastal storms − Coastal soil	Water expansion is decreased due to cooling. Increasing ice melting because of black carbon on snow.

TABLE 1.2
Health effects of climate change. Adapted from references [19], [25].

Gas chromatography with a photo-ionization detector (GC-PID) can be used for simultaneous detection of BTEX compounds in an air sample, but has selectivity problems due to alkane interferences which can result in overestimation of gas concentrations [26], [27].

Gas chromatography with a flame ionization detector (GC-FID) has the advantage of a large linear dynamic range for volatile organic compounds (VOC) analysis. The disadvantage of this method is that it is not able to provide compound confirmation. To overcome this disadvantage it is possible to use two columns with different polarities for simultaneous separation [28]–[32].

Gas chromatography in combination with mass spectrometry (GC-MS) on the other hand has the potential to be portable, making this technique useful for low ppb BTEX measurements [33], [34]. This method has some drawbacks as it can not provide real-time data and is not cost efficient [11]. Regional air quality monitoring programs also use the GC-MS technique. They may take advantage of spatially-resolved data provided by this method, but it is not possible to do real-time measurements as GC-MS uses air samples collected over several days [13], [35], [36].

Other experimental methods for measurement of ppb levels of BTEX gases have been developed, all with their own advantage and disadvantages. Among these methods there is a miniaturized gas chromatography system combined with a solid state metal oxide semiconductor (MOX) detector used to measure BTX concentrations as low as a few ppb [37]. Another technique in this category is GC-ion mobility spectroscopy (IMS) which is able to measure 20 ppb benzene in a BTX gas mixture [38]. However, both techniques suffer from long response times as they are dependent on gas chromatography [11].

On the other hand, membrane introduction mass spectrometry (MIMS) is a method for benzene and toluene detection which does not rely on gas chromatography. The problems which this method can not overcome, include the overlapping between the benzene and toluene peaks as well as not being able to quantify xylenes [39].

In addition to the methods mentioned above, a highly sensitive mass spectrometer was used for monitoring BTEX gases in the atmosphere with direct sampling into the mass spectrometer [36]. Although this method provides real-time measurements, it

is unsuitable for local or regional air quality monitoring because of instrumentation issues. The instruments used in these specialized studies are more difficult to operate due to their size, limited portability, and vibration control and electrical power requirements [13], [36].

Differential optical absorption spectroscopy (DOAS) is an advantageous method for trace gas detection in the atmosphere [40]–[42]. A typical DOAS instrument consists of a continuous light source and an optical setup [3]. In this method, the absorption spectra are transformed to differential optical absorption spectra by fitting a polynomial curve through them. This polynomial is then subtracted from the original absorption spectrum to obtain the differential optical absorption spectrum [40].

Ultraviolet DOAS (UV DOAS) is well-suited for BTEX measurements due to the distinct absorption properties of these gases in the UV range (220-290 nm). The only drawback of the UV DOAS technique is its limitation to path lengths of less than 1 km because of atmospheric attenuation of UV light [40], [42].

Mid-infrared spectroscopy is a technique which is mostly based on absorption measurements. This spectroscopy deals with the mid-infrared region of the electromagnetic spectrum (approximately 400-4000 cm^{-1}), and can be used to identify chemicals [43], [44]. As BTEX molecules selectively absorb infrared light depending on their structures (vibrations between their atom bonds), the molecule specific absorption peaks in an IR spectrum represent a fingerprint of these gases.

Fourier Transform InfraRed (FTIR) spectroscopy is a preferred method of infrared spectroscopy. This method is advantageous as it allows to simultaneously measure a wide range of infrared frequencies. Thus most measurements in this method are made on the order of a few seconds. As the result, it gives better signal to noise ratio (S/N) as it enables averaging several scans and reducing random noise in the same time compared to a dispersive instrument (which separates the individual frequencies emitted from the infrared source using a prism or grating) [45].

Some optical spectroscopy methods use a combination of differential optical absorption spectroscopy (DOAS) with Fourier transform infrared (FTIR) spectroscopy, to measure fairly low (ppb level) concentrations of BTX with accuracy of 30% [46]. DOAS provides continuous and sensitive detection of BTEX compounds, but low

visibility conditions may affect its sensitivity [11]. The selectivity of this technique may suffer from the spectral interferences of BTEX compounds with oxygen, ozone, and several hydrocarbons of similar spectra [36].

Table 1.3 gives a comparison chart of current gas sensing technologies and their advantages and disadvantages.

1.4 Gas Sensor Based on an External Cavity Quantum Cascade Laser (EC-QCL)

In this study, I will be using an External Cavity Quantum Cascade Laser (EC-QCL) as the light source for my measurements and I think it is useful to give a brief introduction to Quantum Cascade Lasers here.

In order to better understand quantum cascade lasers (QCLs), it is good to compare them with a typical diode laser. In a typical semiconductor diode laser, a photon is emitted when an electron from a higher energy level (conduction band) recombines with a hole from a lower energy level (valence band). The wavelength of this emitted light depends on the band gap between these two energy levels, which is material specific.

On the other hand, in a quantum cascade laser a periodic series of thin layers of different materials are used in the optical active region of this semiconductor laser. In this super-lattice only discrete energy levels are allowed. By changing the thickness of these layers, one can tune the energy level spacing and thus the emission wavelength of the laser [47].

In this type of semiconductor lasers, as the electron does not recombine with a hole, once it goes through an intersubband transition and emits a photon in one period of the superlattice, it can move on to the next period of the structure and emit another photon. In this way, a single electron can emit multiple photons which leads to a quantum efficiency of greater than unity and higher output powers than a conventional diode laser [47].

Quantum cascade lasers (QCLs) have opened up a new era in spectroscopic measurements and remote sensing of atmospheric gases. They have been used in several gas sensing applications [48]–[50]. To name a few examples, QCLs have been used in

Detection Method	Advantages	Disadvantages
Gas Chromatography (GC) combined with: a. Photo Ionization Detector (PID) b. Flame Ionization Detector (FID) c. Mass Spectroscopy (MS) d. Solid State Metal Oxide Semiconductor (MOX) Detector	a. Simultaneous detection of BTEX in an air sample b. Large linear dynamic range for VOC analysis; Cost efficient c. Potentially portable; Provides spatially-resolved data d. Measures BTX concentrations at ppb level	Not real-time (uses air samples) and, a. Selectivity problems due to alkane interferences results in overestimation b. No compound confirmation c. Not cost efficient d. Dependent on GC
GC-Ion Mobility Spectroscopy (IMS)	Able to measures 20 ppb benzene in a BTX gas mixture	Long response time (dependent on GC)
Membrane Introduction Mass Spectrometry (MIMS)	For benzene and toluene detection; Not dependent on GC	Overlap between benzene and toluene; not able to quantify xylenes
Highly Sensitive Mass Spectrometer	Direct sampling in the mass spectrometer; Real-time	Instruments difficult to operate (size, limited portability, vibration control and electric power requirements)
UV DOAS	Well-suited for BTEX measurements; Continuous and sensitive detection of BTEX	Limited to path lengths less than 1km due to atmospheric attenuations of UV light
Fourier Transform Infra Red (FTIR) Spectroscopy	Simultaneous measurement of all of the IR frequencies; Fast response; Better SNR	Does not measure spectra; Noise spreads out through the whole spectrum
DOAS combined with FTIR	Able to measure ppb levels of BTX with 30% accuracy; Continuous and sensitive detection of BTEX	Sensitivity and selectivity problems due low visibility conditions and interferences with oxygen, ozone and hydrocarbons with similar spectra

TABLE 1.3
Comparison chart of current gas sensing technologies [3], [11], [13], [26]–[36], [36]–[46].

transmission spectroscopy for atmospheric monitoring [51], as well as in smoke and vehicle emission analysis [52]–[54].

Grating-tuned external cavity quantum cascade lasers were found to meet many

requirements for gas sensing applications, such as narrow laser line width and broadly tunable emission [55], [56]. They typically have tunabilities of 100 cm^{-1} but a 750 cm^{-1} tunability range has been reported [49], [56]–[59].

A schematic diagram of the optical configuration of an EC-QCL [60] is shown in Fig. 1.3.

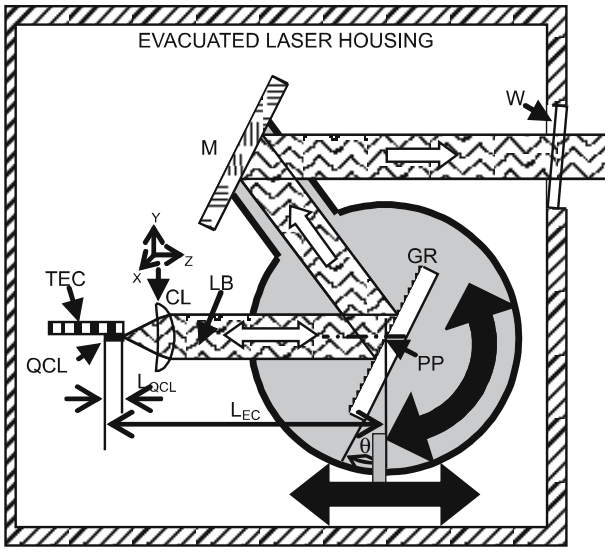

Fig. 1.3. A schematic diagram of the EC-QCL; TEC: thermoelectric cooler, CL: collimating lens, GR: diffraction grating, M: mirror, W: window, PP: the pivot point of the rotational movement, and LB: laser beam [60].

This EC-QCL configuration consists of three main parts: a QCL chip with its thermoelectric cooler (TEC), a collimating lens (CL) with 24 mm diameter, and a diffraction grating (GR). The collimating lens is mounted on a motorized translation stage able to move in three dimensions. The grating is placed on a moving platform which enables independent control of the external cavity length (L_{EC}) and the grating angle. A mirror (M) mounted on the same platform as the grating, reflects the EC-QCL beam to the output window. The laser beam exits the housing through a CaF_2 window (W) with thickness of 4 mm, and tilted by 5° with respect to the normal of the laser beam axis. In Fig. 1.3, PP represents the pivot point of the rotational movement, LB is the laser beam and θ is the incident angle of the laser beam measured between the beam axis and the grating normal [60].

Continuous wave (CW) operation of QCLs at room temperature was achieved in 2002, using a laser with an output power of up to 17 mW at 292 K [61]. Development

of gas sensors based on continuous wave external cavity quantum cascade lasers (CW EC-QCLs) is of great interest due to the broad absorption features of these gases within a specific spectral range [48]. Because of the wide tuning range, EC-QCLs can be used in multiple trace gas detection gas sensors [48].

1.5 Light Scattering by Aerosol Particles

I assume that there are one or more particles placed in an electromagnetic beam of light. If the particles are removed, the power received by the detector is I'_0, while in the presence of particles this power is I', where $I'_0 > I'$. The reduction in power is the result of the extinction effect of the particles on the incident beam. "Extinction is the combined effect of absorption in the particle and scattering in all directions by the particle" [62]. If the medium by which the particles are surrounded is non-absorbing, the difference between I'_0 and I' is just because of absorption and scattering of the particles. Extinction is dependent on several parameters, such as chemical properties, size, shape, orientation and number of the particles as well as the surrounding medium, polarization status and the frequency of the incident beam. Fig. 1.4 shows the incident light extinction by a collection of particles [62].

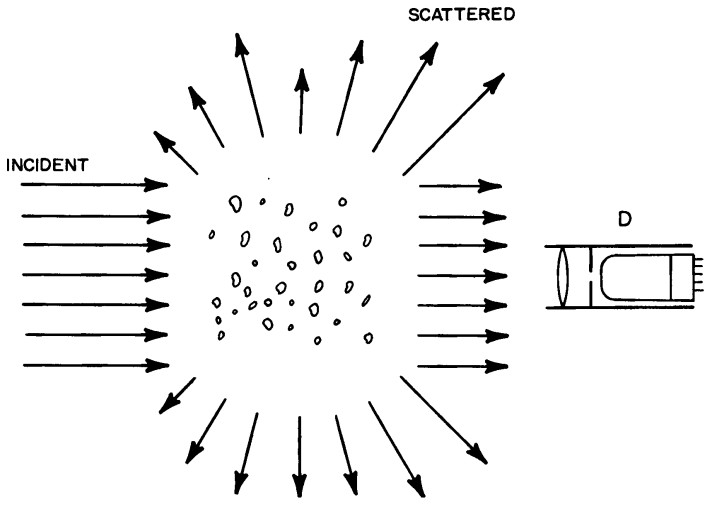

Fig. 1.4. Extinction by a collection of particles [62].

Light scattering from a particle is significantly dependent on the particle refractive index and its diameter. To describe the angular scattering pattern of an aerosol

particle, some definitions are needed. The scattering plane is the plane formed by the incident and scattered beam. The angle between the directions of the incident beam and the scattered beam is called the scattering angle which is in the scattering plane. Scattered light with a small scattering angle is called forward-scattering light while light scattered back to the source is said to be back-scattered light [63].

The two general theories of light scattering by aerosol particles are Mie and Rayleigh scattering. It was in 1908 that Gustav Mie developed a theory which gives the intensity of light scattered by a spherical particle at any scattering angle. The values of refractive index (m) and size parameter of the particle are known. Size parameter of a particle is defined as $2\pi r/\lambda$, where r is the radius of the particle and λ is the wavelength of the incident light. Mie theory is mostly used when the size parameter reaches unity or more accurately when this parameter reaches a value greater than 1/10 [64]. Mie equations get extremely complicated when the size of the particles are larger than the wavelength of incident light [63].

Rayleigh scattering theory is used when aerosol particles are quite small compared to the wavelength λ of incident light. In this case the entire particle is exposed to a uniform electromagnetic field of the incident light. Therefore the particle acts like an oscillating dipole which re-radiates energy in all directions. The total intensity of the light scattered at a distance R, from the particle with a diameter of d, is given by Eq. 1.3 [63].

$$I_s(\theta) = \left(\frac{(I_0 * (\pi^4) * (d^6) * (\frac{m^2-1}{m^2+1})^2 * (1 + (cos(\theta))^2))}{(8 * (R^2) * (\lambda^4)}\right) \tag{1.3}$$

This equation shows that the intensity of scattered light is strongly dependent on the particle diameter and the wavelength of incident light.

The component of scattered light perpendicular to the scattering plane is given by Eq. 1.4 [63].

$$I_1(\theta) = \left(\frac{(I_0 * (\pi^4) * (d^6) * (\frac{m^2-1}{m^2+1})^2)}{(8 * (R^2) * (\lambda^4)}\right) \tag{1.4}$$

And the component of scattered light parallel to the scattering plane is given by Eq. 1.5 [63].

$$I_2(\theta) = (\frac{(I_0 * (\pi^4) * (d^6) * (\frac{m^2-1}{m^2+1})^2 * ((cos(\theta))^2))}{(8 * (R^2) * (\lambda^4)}) \tag{1.5}$$

Consequently, if the diameter of the absorbing particles is much smaller than the wavelength of the incident light, there is no significant change in the light intensity caused by scattering as light beam goes through these particles [63].

In this study, I am using a mid-IR laser system with wavelength range from 9.41-9.88 μm and a UV lamp with wavelength range of 215-400 nm. As benzene, toluene, ethyl-benzene and o-, and p-xylene gases (i.e., BTEX gases) react with hydrogen peroxide inside the simulation chamber, aerosol particles will be formed. These particles mostly have diameter of 50-400 nm. As the diameter of these aerosol particles are much smaller than the mid-IR wavelength, but comparable with the UV wavelength, they should not have any significant scattering effects on the mid-IR laser beam, but they may have noticeable scattering effects on the UV beam.

1.6 Thesis Overview

In this work, I demonstrate progress in developing an application of a tunable mid-IR continuous wave external cavity quantum cascade laser (EC-QCL) absorption spectroscopy for simultaneous concentration measurements of multiple trace gas species.

Benzene, toluene, ethylbenzene and o- and p-xylene (i.e. BTEX) gas concentrations were measured simultaneously during a series of aerosol formation processes simulated in a photoreaction chamber ("smog chamber"). The results are compared with concurrent in situ measurements of the trace gas concentrations with a UV absorption spectrometer as a confirmation.

The experimental setup and methods used in this study are described in Chapter 2. Results obtained in the experiments are discussed in Chapter 3. Chapter 4 is the conclusion part which gives a summery of what has been done and an idea of future work.

At the time I joined this project, the photoreaction chamber, UV and mid-IR first system were all setup and calibration measurements along with other experiments with benzene, toluene and p-xylene were also done. My contributions to this project include repeating these calibration measurements using the existing mid-IR system,

and performing calibration measurements for two additional compounds, namely o-xylene and ethylbenzene. Finally I decided to put all five compounds (benzene, toluene, ethylbenzene, o- and p-xylene) together in the photoreaction chamber to see if I am able to distinguish between these gases despite overlaps between their peaks. Having done two multiple measurements with all five compounds, I decided to extend the path length of the mid-IR system from 70 m to 100 m, to increase the sensitivity of the system and decrease the uncertainty and detection limit. I did the calibration measurements for this new mid-IR system and also one multiple compound test with all five compounds. Afterwards, I improved the mid-IR system by adding another detector and also increase the path length, slightly from 100 m to 110 m. With this new setup, I am able to measure real-time reference spectra for the concentration measurements to address the changes in the laser output during the experiment and even scan to scan. The path length extension also increased the sensitivity of the mid-IR system. After going through the calibration measurements for this new mid-IR system, I did three more multiple compounds measurements with all five compounds.

Beside all these experiments, I have also contributed in few measurements using a particle sizer to determine the size of the particles being made inside the photoreaction chamber during the reaction of BTEX with hydroxyl radicals.

Chapter 2

Methods

As described in chapter 1, the objective of this project is to detect benzene, toluene, ethylbenzene, o-, and p-xylene, known as BTEX gases, and determine their concentrations during real-time monitoring of their chemical reaction with hydroxyl radicals, which are produced when H_2O_2 is exposed to UV radiation.

2.1 Experimental Setup

The experimental setup used in this study consists of three main parts: photoreaction chamber, UV system and mid-IR system. The photochemical reactions take place inside the chamber and two different detection systems (UV & mid-IR) are used to monitor the BTEX concentrations at the same time.

Fig. 2.1 shows a schematic diagram of this setup. A detailed description of the major components of the experimental setup can be found below.

2.1.1 Photoreaction Chamber

The photoreaction chamber is a cube constructed of 0.127 mm thick perfluoroalkoxy (PFA) film with a volume of 1.8 m^3 (Ingeniven Fluoropolymer Solutions) supported by an aluminum enclosure.

The chamber can be irradiated with UV light by an array of 24 fluorescent 32 W black lights with peak emission at 350 nm. The spectrum of these black lights is shown in Fig. 2.2.

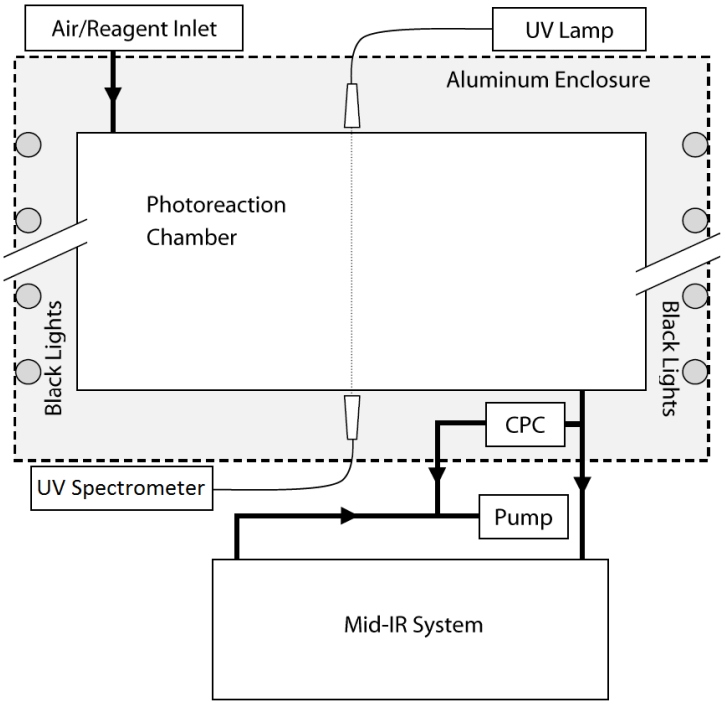

Fig. 2.1. Schematic diagram of the experimental setup.

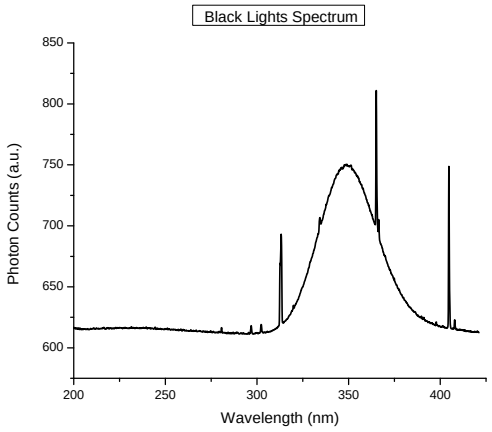

Fig. 2.2. UV black light spectrum.

Inlet and outlet tubing of the photoreaction chamber are made of PFA, conductive PFA, or stainless steel where appropriate (conductive silicone tubing was found to interfere with toluene sampling, and was therefore not used [13]). As seen in the block diagram shown in Fig. 2.1, there is an inlet to admit dry air or reagent gas into the photoreaction chamber while the outlet is connected to the condensation particle counter (CPC (TSI, 3771)) and the mid-IR system input. The exhaust flow

coming from both CPC and mid-IR system outputs are directed to a pump.

A condensation particle counter is installed at the outlet of the photoreaction chamber, inside the aluminum enclosure to operate at the same temperature as the photoreaction chamber. It monitors the total particle number density inside the photoreaction chamber continuously and can detect particles with diameters greater than 10 nm [13].

A schematic diagram of this condensation particle counter is shown in Fig. 2.3 [65].

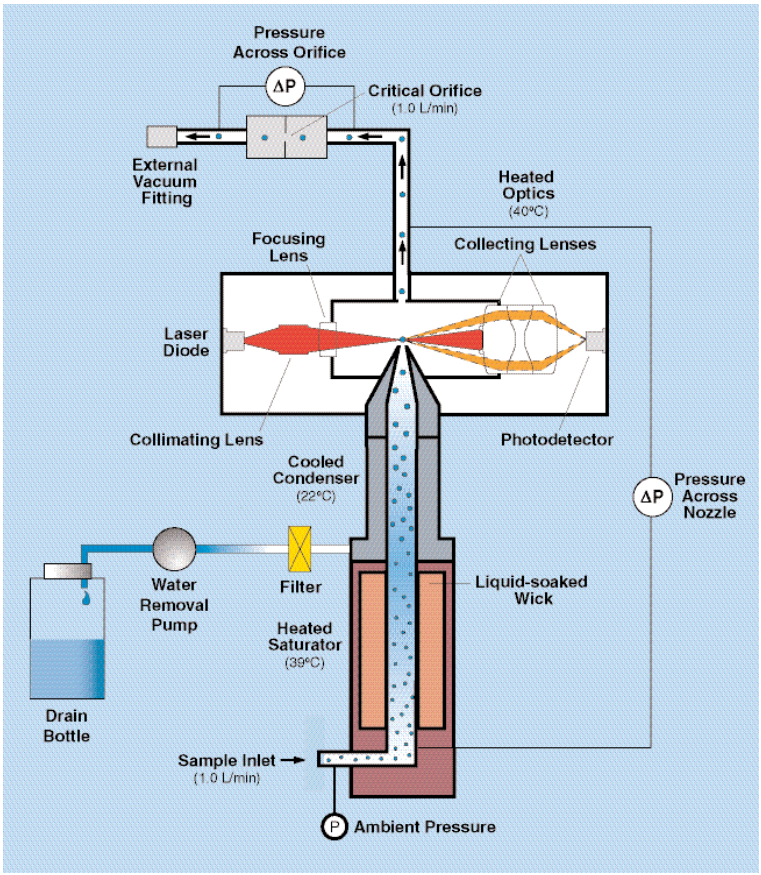

Fig. 2.3. Schematic diagram of condensation particle counter [65].

A brief description on how the CPC detects particles is given below. The sample flow from the photoreaction chamber is drawn continuously through a heated saturator in which alcohol is vaporized and diffuses into the sample stream. Then, by passing through a cooled condenser, the alcohol vapor becomes supersaturated and ready to condense on the aerosol particles in the sample stream which serve as condensation nuclei. Once condensation begins, particles with diameter larger

than a threshold grow quickly into larger droplets which can then be counted easily by passing through an optical detector as shown in Fig. 2.3. The detector counts individual pulses produced as each droplet passes through the sensing zone.

The other measuring instruments used in this setup include pressure monitor, mass flow meter (MFM), mass flow controller (MFC), and temperature and relative humidity monitors which were installed on or under the aluminum enclosure.

A mass flow controller is installed on the inlet port to the photoreaction chamber and is connected electronically (voltage) to the mass flow meter, which is attached to the outlet port to monitor the flow from the chamber. The measured flow at the outlet port was used to determine the set-point for the mass flow controller at the inlet. This system was set up as a negative feedback loop to adjust the flow through the mass flow controller in order to avoid inflating or deflating the chamber.

Temperatures were measured on the outer surface of the photoreaction chamber and at the outside of the aluminum enclosure. Typically temperatures during the experiments were around 25-30 °C and 21 °C, respectively.

2.1.2 UV System

The UV system used in this study is made of two main parts, a light source and the spectrometer. The light source for UV differential optical absorption spectroscopy is a broad band deuterium lamp (Ocean Optics, D-2000-S) with output from 215-400 nm. Fig. 2.4 shows the output spectrum of the UV lamp used in this study.

The measurement system is a grating-based UV spectrometer (Ocean Optics, HR-2000+) with a spectral resolution of 0.118 nm. The UV spectrometer was factory calibrated. Additional quality checks were performed periodically by measuring the wavelengths of several discrete emission lines from the fluorescent black lights to ensure consistency in the wavelength calibration of the UV spectrometer over time. Wavelength drifts in the UV spectrometer were not observed in this study [13].

Fig. 2.5 illustrates how the light passes through this UV spectrometer. The function of each numbered component in the diagram shown in Fig. 2.5 is as follows. SMA connector: light from the input fiber enters the optical bench through this connector. Slit: a dark rectangular aperture placed right after the connector. The amount of light entering the optical bench and the spectral resolution can be

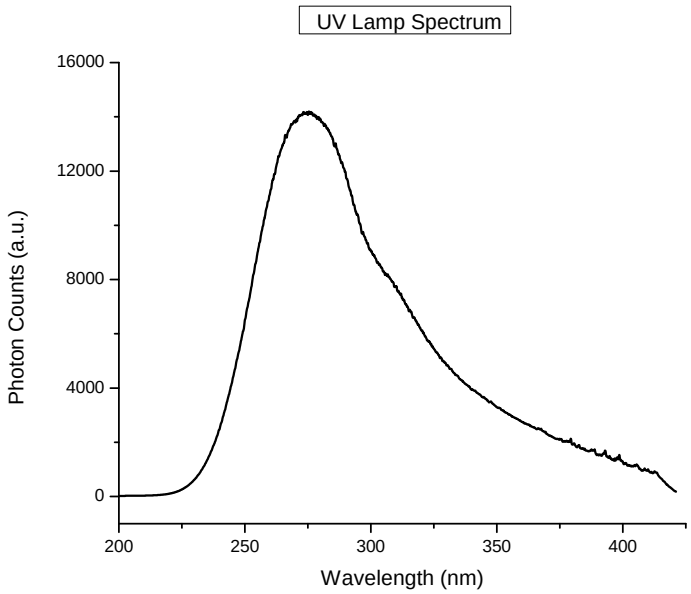

Fig. 2.4. UV lamp output spectrum.

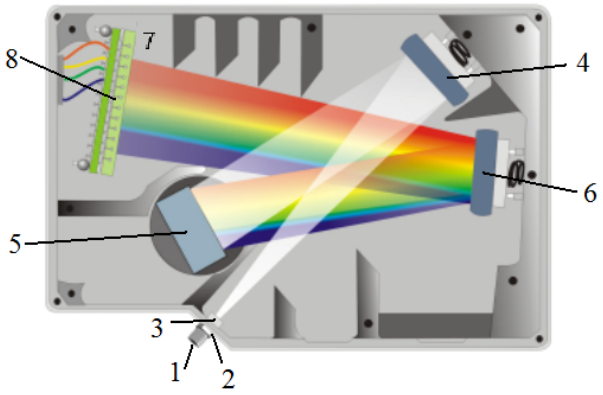

Fig. 2.5. Schematic diagram of the UV spectrometer; 1. SMA Connector, 2. Slit, 3. Filter, 4. Collimating Mirror, 5. Grating, 6. Focusing Mirror, 7. L2 Detector Collection Lens, 8. CCD Detector [66].

controlled by the aperture size. Filter: both bandpass and long-pass filters are available to restrict radiation to certain wavelength regions. Collimating Mirror: collimates the light entering the optical bench and reflects it towards the grating of the spectrometer. Grating: diffracts light from the collimating mirror and directs the diffracted light onto the focusing mirror. The grating determines the wavelength coverage and resolution of the spectrometer. Focusing Mirror: focuses the light onto the CCD detector or detector collection lens. Detector Collection Lens: an optional component attached to the CCD detector which focuses light from a tall slit onto

the shorter CCD detector elements. CCD Detector: converts the optical signal into a digital signal.

An optical fiber and a collimating lens were used to direct the UV light from the deuterium lamp through the photoreaction chamber. Likewise, a collecting lens and optical fiber were used to direct the UV light into the UV spectrometer. No windows were required since the PFA film is transparent to UV. The deuterium lamp and the UV spectrometer were positioned outside the aluminum enclosure of the photoreaction chamber and maintained at a temperature of approximately 21 °C.

All UV absorption spectra were referenced to filtered, dry air at the start of each experiment.

2.1.3 Mid-IR System

The mid-IR laser system used in these measurements is made of four main parts: an external cavity quantum cascade laser (EC-QCL) system, a multipass cell, an alignment setup and the detection system. Two different configurations were used in this work: a single detector setup and a double detector setup, as shown in Fig. 2.6.

2.1.3.1 Single Detector Setup

The mid-IR single detector setup is shown in Fig. 2.6. In this diagram, BS represents a beam splitter and MCT represents a liquid nitrogen cooled mercury cadmium telluride IR detector. The function of each component in Fig. 2.6 is described below.

A room temperature continuous wave external cavity quantum cascade laser (Daylight Solutions, TLS-CW-MHF), tunable between 9.41 and 9.88 μm with mode hop free tunability from 9.68-9.88 μm (1012-1032 cm^{-1}) was the light source for the measurements described in this thesis.

The output of the EC-QCL over the entire tuning range before and after smoothing is shown in Figs. 2.7 & 2.8.

The tunable range of this EC-QCL lies in one of several regions with minimal interference from common atmospheric species, such as CO_2 and water. The wavelength of the EC-QCL is calibrated periodically by the wavelength of several discrete

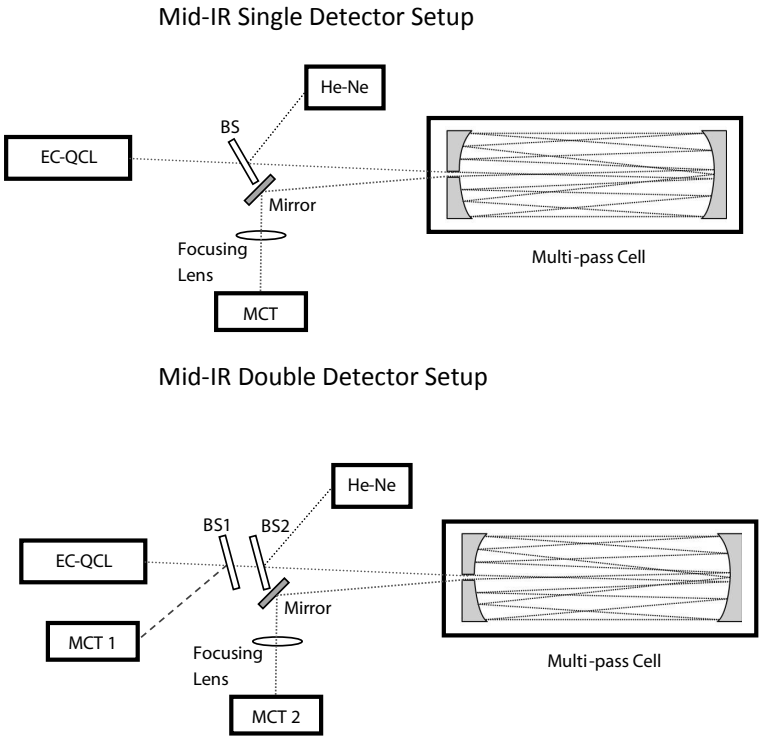

Fig. 2.6. Schematic diagram of mid-IR setup.

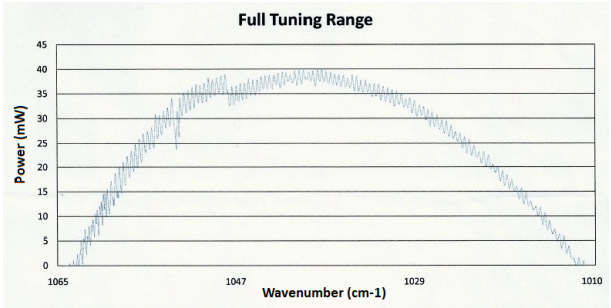

Fig. 2.7. Output of the EC-QCL over the entire tuning range before smoothing.

absorption lines in a pure CO_2 gas sample to ensure measurement consistency over time. The maximum laser output power is 40 mW and the laser beam divergence is $<$5 $mrad$. The maximum tuning rate of the laser is 5 cm^{-1}/s [13]. The laser head temperature is controlled using a thermoelectric cooler (TEC) and was typically set to 16.8 °C. The laser case temperature was also maintained at around 16.8 °C using chilled water recirculation.

As it is impossible to see the IR beam pattern on multipass cell mirrors, a HeNe laser was used to make the beam pattern visible. A beam splitter was used between

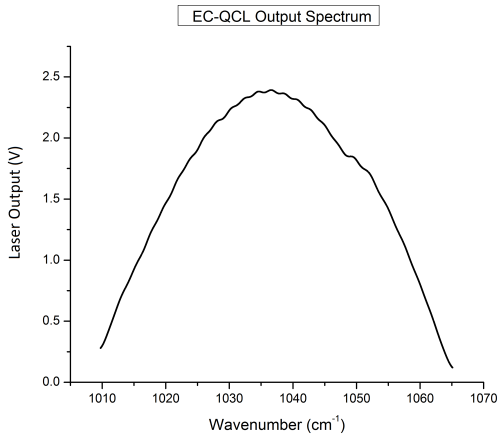

Fig. 2.8. Output of the EC-QCL over the entire tuning range after smoothing.

the EC-QCL output and the multipass cell as shown Fig. 2.6. This beam splitter which passes the IR beam completely while splitting the HeNe beam with 50/50 ratio, was used in order to align the multipass cell. The HeNe laser beam was adjusted to be coaxial with the EC-QCL beam. The system alignment is described in detail later.

The laser beam exiting the beam splitter was directed into an astigmatic Herriott multipass cell [67] mounted in a vacuum tight aluminum chamber with a volume of approximately 14.2 L and a 50.8 mm diameter ZnSe window installed on its front flange. There is one inlet for sample gas on the rear flange and one outlet for exhaust flow on the front flange of multipass cell.

The multipass cell consists of astigmatic mirrors (Aerodyne Research, Inc.) with diameter of approximately 76 mm and a 5.3 mm input coupling hole in the center of the front mirror. The mirrors which are shown in Fig. 2.9, have a broad band dielectric coating and a reflectivity of approximately 99.2 %. Two configurations were used for the multipass cell, one with 70 m path length and the other with 100 m path length. The mirrors inside the multipass cell are separated by about 55 cm and 182 passes give a total path length of approximately 100 m. The gage on the multipass cell input displays its inside pressure, which was desired to be at 1 atm.

In order to align the optical components, an IR camera was used to help visualizing the mid-IR beam. First of all, the height of the EC-QCL beam was adjusted so that it is centered on the multipass cell input hole. After that, the multipass cell was

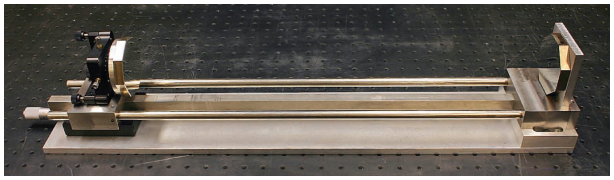

Fig. 2.9. Mid-IR multipass cell.

removed to give more space and a beam splitter was installed next to the EC-QCL output. This beam splitter passes the mid-IR beam completely while splitting the HeNe beam with a 50/50 ratio.

By adjusting the alignment angle of the beam splitter, the HeNe and the mid-IR beams were made to overlap at three different points: near the EC-QCL output right after the beam splitter, at the multipass cell entrance and at the position of multipass cell rear mirror. When the two beams are coaxial, the HeNe beam can help tracking the mid-IR beam through the multipass cell and out to the detector.

Afterwards, the multipass cell was put back in its place and by changing its angle and adjusting its back mirror, the desired spot pattern of the mid-IR beam on the mirrors and path length could be achieved. A sample laser spot pattern on the multipass cell rear mirror with approximately 180 passes is shown in Fig. 2.10.

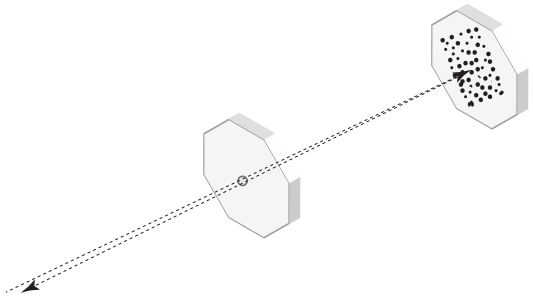

Fig. 2.10. A sample laser spot pattern on the rear mirror of the multipass cell.

A mirror with reflectivity of 99% was used to direct the beam exiting the multipass cell to a focusing lens with 25.4 mm diameter and focal length of 38 mm [68]. This lens was then used to focus the beam onto the active area of a liquid nitrogen cooled mercury cadmium telluride (MCT) photovoltaic IR detector (Kolmar Technologies, KMPV11). The detector output was then digitized and transfered to a personal computer to be analyzed.

2.1.3.2 Double Detector Setup

In the double detector setup shown in Fig. 2.6, a second detector and another beam splitter were used to improve the performance of the mid-IR system by providing a real time reference signal. In this diagram, BS1 & BS2 are ZnSe beam splitters and MCT1 & MCT2 represent the liquid nitrogen cooled IR reference and sample detectors, respectively.

In the single detector setup, a reference spectrum was stored at the beginning of each measurement and it was used as the reference throughout the measurement period. However, the laser output power can change from time to time and even from scan to scan, such that it does not provide the exact same spectrum as at the beginning of the measurement. Referring to only one initial reference spectrum adds substantial noise to the data. In order to reduce the noise and also decrease the detection limit, a second detector was used to provide real-time reference spectra. To achieve this, a second beam splitter (BS1) with 50/50 ratio was used to split the mid-IR beam right after it exits the EC-QCL output into two mid-IR beams with half intensity and direct one of them into the second mid-IR detector (MCT1).

The maximum laser power right after exiting the laser cavity is 40 mW. After the first beam splitter (BS1), which has 50% reflectivity and 50% transmission, the laser power is 20 mW. As the second beam splitter (BS2) only splits the HeNe beam and passes the mid-IR beam completely, the laser power before entering the multipass cell is around 20 mW. The mirrors inside the multipass cell have 99.2% refletivity, which means the laser power is reduced by 0.8% each time it reflects back from these mirrors. The max laser power after exiting the multipass is around 35%, 23% and 20% of the power of the initial laser beam (20 mW), due to the losses inside the 70 m, 100 m and 110 m path length multipass cell configurations, respectively.

The two MCT IR detectors are not completely identical. Thus, in order to be able to use the spectra from the reference detector as real-time reference spectra, C(λ) was stored at the beginning of each experiment. C(λ) is the ratio of the amplitude of the reference spectrum to the amplitude of the sample spectrum at the beginning of the experiment. Later on, C(λ) was used to convert the reference spectra to the real-time reference spectra for the sample data. See Eq. 2.4 for further details.

2.2 Spectroscopic Methods

2.2.1 Spectroscopy

In order to better understand how light can be used in identification and quantification of trace molecular species, it is important to know the fundamentals of absorption. The Beer-Lambert law [69] describes the relation between light absorption by a material and the material properties. The absorbance (A) is shown in Eq. 2.1 [70]. In this Eq. $I = I_{signal} - I_{dark}$ and $I_0 = I_{ref.} - I_{darkref.}$. I_{signal} is the intensity of the light beam after it passes through the sample gas and $I_{ref.}$ is the intensity of the light beam after it passes through the reference gas (e.g. filtered, dry air). In the mid-IR double detector setup, $I_{ref.}$ is measured by the reference detector during the measurement. I_{dark} is the detector response without any light beam directed to it. In the mid-IR double detector setup, $I_{darkref.}$ is the reference detector response with no light beam directed to it. The dark spectra were subtracted from the corresponding reference and sample spectra to obtain more reliable absorbance measurements.

$$A = -\log_{10}\left(\frac{I}{I_0}\right) = \epsilon c l \tag{2.1}$$

l represents the path length which light travels through the material, ϵ is the molar absorptivity (extinction coefficient) of the material and c is the molar concentration of the absorbing species.

The transmission, T, is defined as

$$T = \frac{I}{I_0} = e^{-\alpha l} = e^{-\sigma l N} \tag{2.2}$$

For gas concentration measurements, the natural logarithm is often used to obtain the absorbance:

$$A' = -\ln(\frac{I}{I_0}) = \sigma l N \tag{2.3}$$

σ is absorption cross section of the absorbing material and N is the number density (number per unit volume) of the absorbing particles.

If a sufficient path length is provided, it is possible to detect the concentration of

BTEX gases at trace levels (ppb or ppm). Beer's law shows a linear relation between absorbance and concentration ($A' = \sigma l N$) at a constant path length [11].

In both mid-IR and UV systems, the raw spectra were transfered to a personal computer to be analyzed there. In this analysis process, the UV raw data were transformed to absorption spectra using Eq. 2.3. In Eq. 2.3, A represents absorption, I is the intensity of the UV light after passing through the photoreaction chamber containing BTEX gases and I_0 is the measured intensity without any absorber.

The mid-IR raw data on the other hand, were transformed to the absorbance spectra using Eq. 2.1. In Eq. 2.1, A is the mid-IR laser light absorbance through the BTEX gases inside the multipass cell, I is the intensity of the laser light after it passes through the gas sample and I_0 is the intensity of the light after it passes only through filtered, dry air inside the multipass cell.

In the two detector mid-IR setup, reference spectra come directly from the reference detector and the absorbance is calculated using Eq. 2.4.

$$\begin{aligned} C(\lambda) &= \frac{I_0(\lambda, 0)}{I(\lambda, 0)} \\ I'(\lambda, t) &= \frac{I_0(\lambda, t)}{C(\lambda)} \\ A &= -\log\left(\frac{I(\lambda, t)}{I'(\lambda, t)}\right) \end{aligned} \tag{2.4}$$

Here, $C(\lambda)$ is the ratio of the amplitude of the reference spectrum to the amplitude of the sample spectrum, which is stored at the beginning of each measurement with only reference gas (N_2 in calibration tests and filtered, dry air in other tests) in the multipass cell. We use $C(\lambda)$ to correct for the different responses of reference detector and sample detector during the experiments. $I_0(\lambda, 0)$ and $I(\lambda, 0)$ are reference and sample spectra stored at the beginning of each measurement with only reference gas in the multipass cell, respectively. $I_0(\lambda, t)$ is the reference detector spectrum at a given time t, and $I'(\lambda, t)$ is the converted reference spectrum at time t which is used as reference.

2.2.2 Differential Optical Absorption Spectroscopy (DOAS)

Figs. 2.11 & 2.12 show reference spectra in the mid-IR 110 m and UV systems. The absorption/absorbance spectra from the UV/mid-IR systems were obtained using reference and sample spectra at each time and were then transformed to the differential optical absorption spectra as described below.

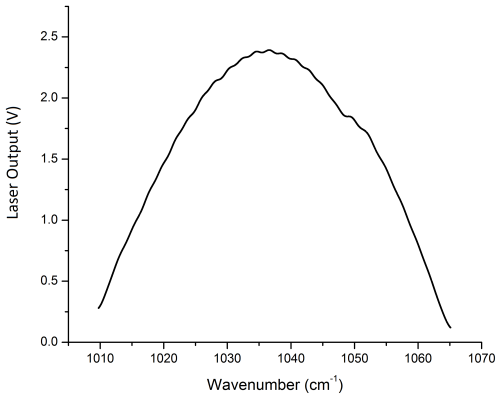

Fig. 2.11. A reference spectrum for the mid-IR 110 m system with only air in the mid-IR multipass cell.

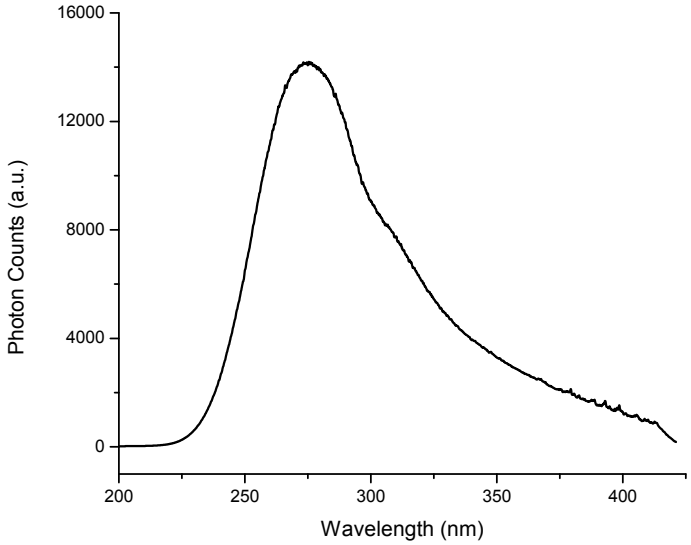

Fig. 2.12. A reference spectrum for the UV system with only air in the photoreaction chamber.

Each absorption/absorbance spectrum (an example is given in Fig. 2.13) was

fit to a ninth or seventh order polynomial over the region of interest (240-286 nm for UV, and 1011-1050 cm^{-1} for mid-IR) (Fig. 2.14). The polynomial was then subtracted from the original absorption/absorbance spectrum, in order to remove the temporal drifts in the light source output power (Fig. 2.15).

The resulting differential optical absorption spectra were fit to literature data of absorption cross sections [71], [72] using a least squares fitting method (Fig. 2.16). This process was repeated seven times and the results of each iteration were used as the starting point for the next iteration in order to determine the observed concentrations of each reagent gas. The reason for choosing seven iterations is that the concentration results reach a stable point after these many times.

Literature absorption cross section data at 293°K with a resolution of 0.001 nm [72] were used for the UV data analyses. Literature absorption cross section data at 298°K with a resolution of 0.06 cm^{-1} [71] were used for the mid-IR data analyses. The literature data were interpolated to the same wavelength scale used in this study and then smoothed with a cubic spline fit during the fitting routine. We have not considered temperature effects in this study as spectral fluctuations caused by small variations in temperature are within the uncertainty limits for literature [71], [72] and measured spectral data.

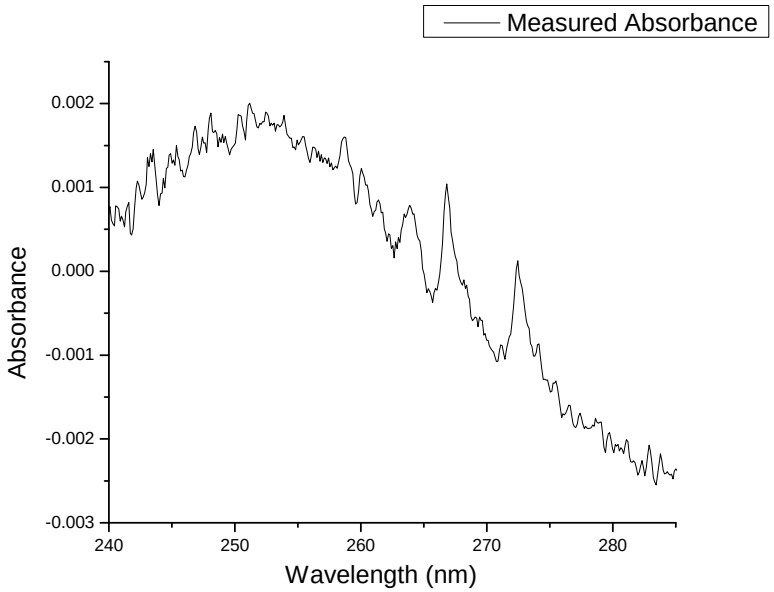

Fig. 2.13. Observed absorbance spectrum of a sample (p-xylene).

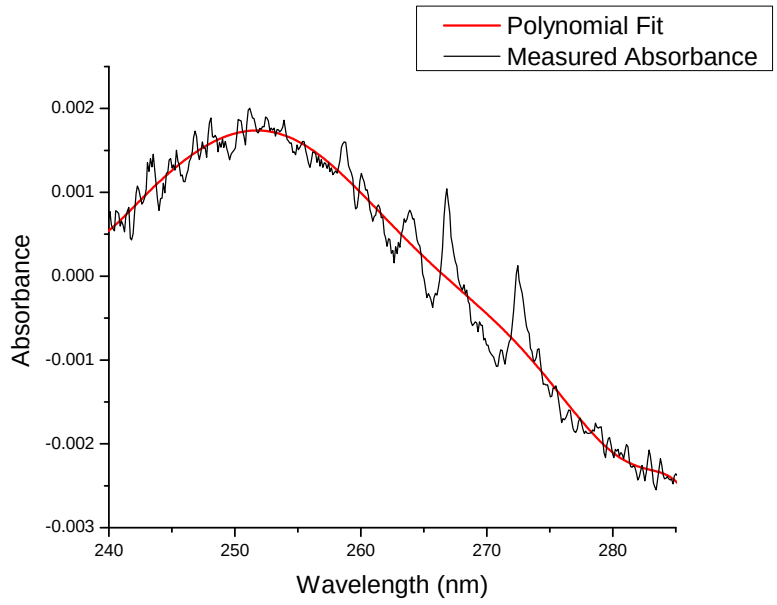

Fig. 2.14. Observed absorbance spectrum of a sample with its polynomial fit.

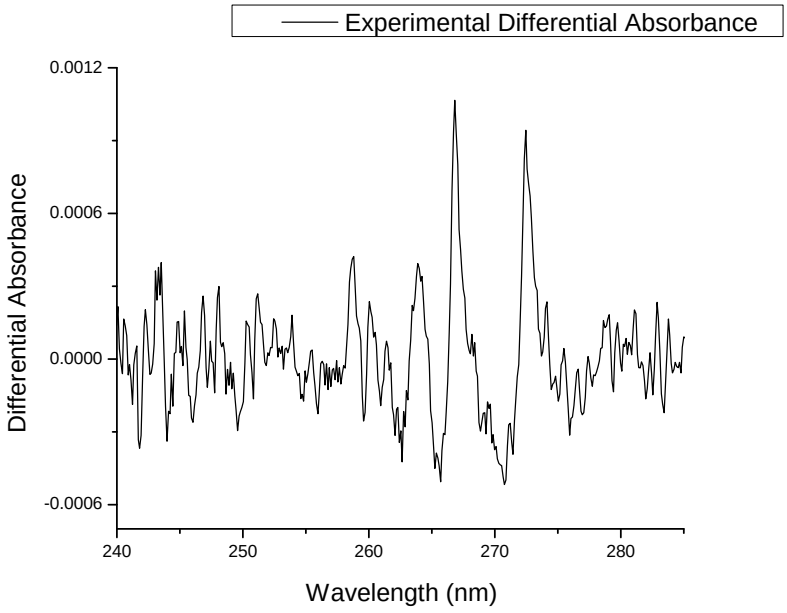

Fig. 2.15. Experimental differential absorbance spectrum of a sample.

2.2.3 Data Correction

In order to account for problems associated with extractive measurements with the mid-IR system such as systematic errors, interferences, losses, and uncertainties related to the sampling process, the observed gas concentrations from the literature

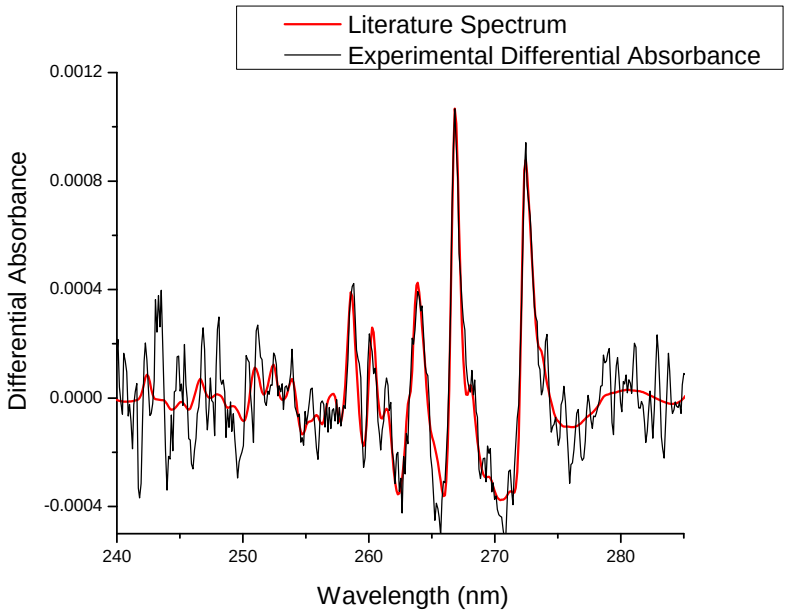

Fig. 2.16. Experimental and literature differential absorbance spectrum of a sample.

fitting results were converted to actual gas concentrations using a calibration method.

If the results needed to be corrected for dilution effects, Eq. 2.5 was used. Please refer to Section 2.3 for more detail on dilution effects.

$$C^{'}(t) = \frac{C(t)}{\exp\left(-\frac{Q(t)\cdot t}{V}\right)} \tag{2.5}$$

Here, $C^{'}(t)$ is the dilution corrected concentration of a component inside the photoreaction chamber at time t, $C(t)$ is the actual measured concentration of that specific component inside the photoreaction chamber at time t, $Q(t)$ is the volumetric flow rate of air entering and exiting the photoreaction chamber at time t, and V is the volume of the chamber ($1844 \pm 100\ L$).

2.3 Experiments

All experiments, except for the calibration measurements, were carried out with filtered, dry air diluting the contents of the photoreaction chamber while sampling from the chamber in order to keep its volume constant. Flow rates during the experiments were usually approximately 1.5-3.5 standard litre per minute ($SLPM$)

and when flushing approximately 10 $SLPM$.

BTEX gases [benzene (Caledon, 99 %), toluene (Fisher Scientific, 99.9 %), ethylbenzene (Fisher Scientific, 99.8 %, o-xylene (Sigma Aldrich, 97 %) and p-xylene (Fisher Scientific, 99.9 %)] were introduced into the photoreaction chamber in two different ways. For injection of benzene and toluene, I used a glass bubbler, shown in Fig. 2.17, which is installed underneath the photoreaction chamber outside the aluminum enclosure. A flow of filtered, dry air over a liquid reservoir of these reagents was used to inject the gases into the photoreaction chamber. The reservoirs were maintained at a temperature of approximately 21°C. For ethylbenzene, o-, and p-xylene I used a microlitre syringe and injected the liquid directly into the chamber. After that, the chamber was sealed over night before the measurement to let the liquid evaporate inside the chamber. This provides sufficient time for the BTEX gases to diffuse and mix before the experiment starts.

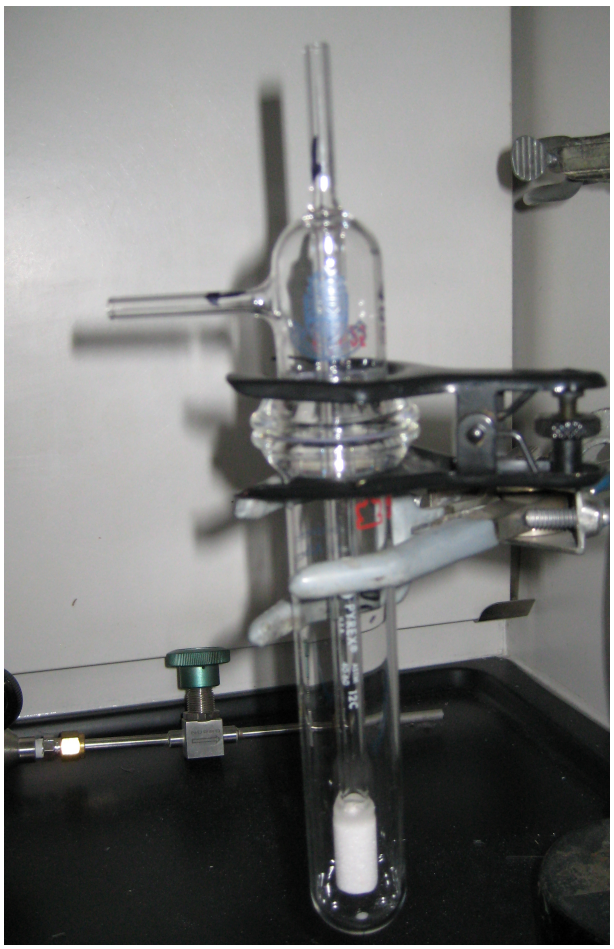

Fig. 2.17. Glass bubbler.

Another glass bubbler was used to continuously supply the photoreaction chamber with H_2O_2 (Fisher Scientific, 30% (W/W) in water) during the experiment, via a flow of filtered, dry air over the H_2O_2 liquid reservoir. I let the gases inside the chamber mix with H_2O_2 for 30 min before turning on the black lights in order to start the aerosol formation. The time at which the black lights were turned on defines time t = 0 min. Following each experiment, the photoreaction chamber was flushed with approximately 10 $SLPM$ of filtered, dry air and H_2O_2 gas while irradiated with the UV lights for at least 24 h, and then flushed without UV exposure using only filtered, dry air for at least 24 h.

A complete list of experiments carried out in this study and their objectives can be found below. These experiments include: calibration, preliminary, single compound, double compound and five compound measurements.

2.3.1 Calibration Measurements

Calibration measurements were done in order to be able to convert the gas concentration determined from the UV and mid-IR experimental data to the actual gas concentrations. For this, a calibration gas generator (Kin-Tek 491-MB) was used. This calibration gas generator provides a constant emission rate of a sample gas (benzene, toluene, or o-xylene) from a permeation tube at a specific temperature (50°C, 80°C, and 100°C for benzene, toluene, and o-xylene, respectively). The concentration of the sample gas can then be adjusted based on the flow rate of diluent gas (N_2) between $0.1 - 5$ $Std\ L \cdot min^{-1}$.

For the UV system calibration, a separate single pass sample cell (path length of 0.5 m, and volume of approximately 0.25 L) was used. The photoreaction chamber was not used to calibrate the UV system because it would take up to 300 h in some cases to fill the photoreaction chamber at the slow flow rates from the calibration gas generator.

All the mid-IR single detector and double detector setup calibration experiments were done using a multipass cell with three configurations for path length (70, 100 and 110 m) and N_2 background. Teflon tubing was used to carry the sample gas from the Kin-Tek calibration gas generator to the multipass cell. The measurements were carried out at room temperature and 1 atm pressure.

In the single detector setup with 70 m path length, the multipass cell was sealed once it was filled with N_2 background gas in order to measure and store the reference spectrum. The calibration gas generator was connected to the multipass cell, set to the desired temperature and to the desired flow rate. The flow rate for the desired gas concentration can be calculated using Eqs. 2.6, 2.7 and 2.8 for benzene, toluene and o-xylene, respectively.

$$F_B = \frac{0.287 * 1.879}{\text{Benzene Concentration (ppm)}} \tag{2.6}$$

$$F_T = \frac{0.243 * 2.263}{\text{Toluene Concentration (ppm)}} \tag{2.7}$$

$$F_O = \frac{0.211 * 2.548}{\text{o-Xylene Concentration (ppm)}} \tag{2.8}$$

The gas flow from the calibration gas generator through the multipass cell and out to the fume hood was kept constant to maintain a constant pressure inside the multipass cell. In this set of measurements, I have used benzene and o-xylene at concentrations of 0.5, 1, 2, and 3 ppm.

In the single detector setup with 100 m path length, the calibration gas generator was used to provide the N_2 flow. This made it possible to adjust the N_2 flow going into the multipass cell. Once the multipass cell was filled with N_2 at a pressure of 1 atm, I adjusted the flow rate on the calibration gas generator to be the same as the flow rate for the sample gas which was supposed to be measured. If multiple concentrations were to be measured, the fastest flow corresponding to minimum concentration was chosen as reference flow rate. Choosing the reference flow rate to be the same as the flow rate used for the gas concentration measurements, reduced the noise in the system and provided more accurate results. Again, benzene, toluene, and o-xylene were used for these calibration measurements.

In the double detector setup with 110 m path length, however, a different setup with two detectors, one for the sample spectra and other for the reference spectra, was used. At the beginning, I stored the dark spectrum (the detector response with laser shutter closed) and the reference simultaneously and at the same flow rate

as was used to achieve the desired gas concentration in the corresponding sample measurement. Also in this case, benzene, toluene, and o-xylene were used with concentrations in the range of 0-5 *ppm* with 0.5 *ppm* steps. The resulting calibration curves will be discussed in detail in Chapter 3.

2.3.2 Preliminary Measurements

The experimental setup containing both UV and mid-IR (70 m path length) systems has been used previously for real time detection of benzene, toluene, and p-xylene [13], [48]. In this step I wanted to explore the possibilities to detect ethylbenzene and o-xylene using the same setup. I conducted a set of preliminary experiments, which are discussed in detail in this section.

Starting with single compound measurements (ethylbenzene, o-xylene), I moved forward to two compounds measurements and then to five compounds measurements (benzene, toluene, ethylbenzene, o-xylene, p-xylene) to study their spectral interferences and see if it is even possible to detect all five compounds together.

2.3.2.1 Single Compound Measurements

In these sets of measurements, ethylbenzene or o-xylene were measured using both UV and mid-IR systems in real time as they react with the OH radicals produced from hydrogen peroxide (H_2O_2). As shown in Figs. 2.18 & 2.19, both ethylbenzene and o-xylene have weak peaks in the UV and mid-IR regions of our interest. Being able to detect these weak signatures would validate this study. Each experiment with only ethylbenzene or o-xylene was repeated once to confirm the results. The resulting spectra will be discussed in more details in Chapter 3.

2.3.2.2 Double Compound Measurements

In the double compounds experiments, ethylbenzene and o-xylene were mixed in the photoreaction chamber and their concentrations were monitored using the UV and mid-IR systems. The concentrations of these compounds decay exponentially during their reaction with the OH radicals. As can be seen in the ethylbenzene and o-xylene spectra in Figs. 2.18 & 2.19, there is no significant overlap of the absorption features of these two gases in both UV and mid-IR regions. This makes identification and

quantification of these two compounds less difficult. Again here, each experiment was repeated to make sure that the results are reproducible. The results will be discussed in more detail in Chapter 3.

2.3.3 Five Compound Measurements

After the preliminary measurements, I carried out more complex experiments. All five BTEX species were mixed together in the photoreaction chamber to study their concentrations as they undergo photochemical reactions with hydroxyl radicals in the presence of H_2O_2 and UV light. Figs. 2.18 & 2.19 show benzene, toluene, ethylbenzene, o-, and p-xylene spectra in both mid-IR and UV ranges.

By taking a more detailed look, one could point out significant interference between ethylbenzene and toluene peaks as well as between p-xylene and o-xylene peaks, in particular in the mid-IR region. This was the main concern while monitoring these gases at low concentrations.

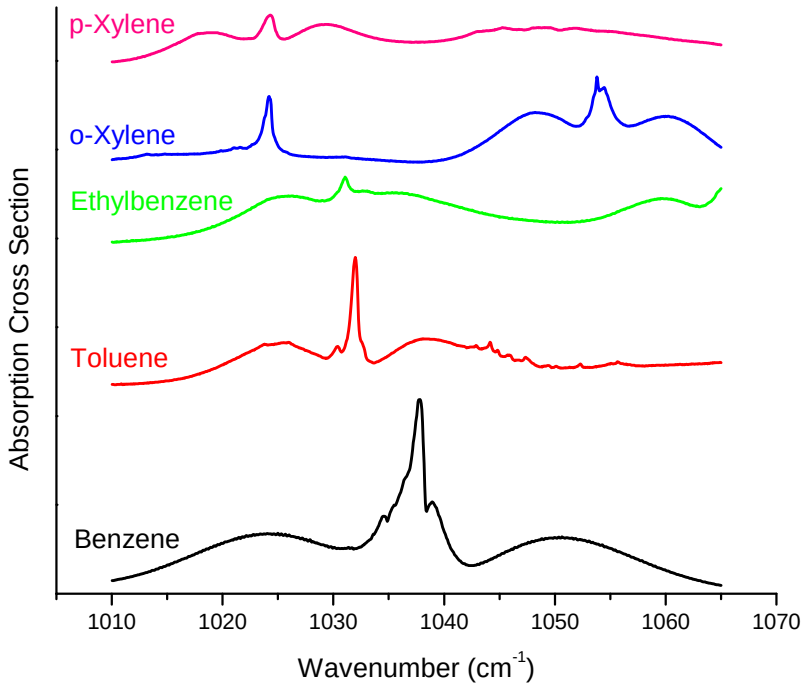

Fig. 2.18. Benzene, toluene, ethylbenzene, o-, and p-xylene spectra in the mid-IR region [71].

Three different configurations of the mid-IR system with 70, 100 and 110 m path

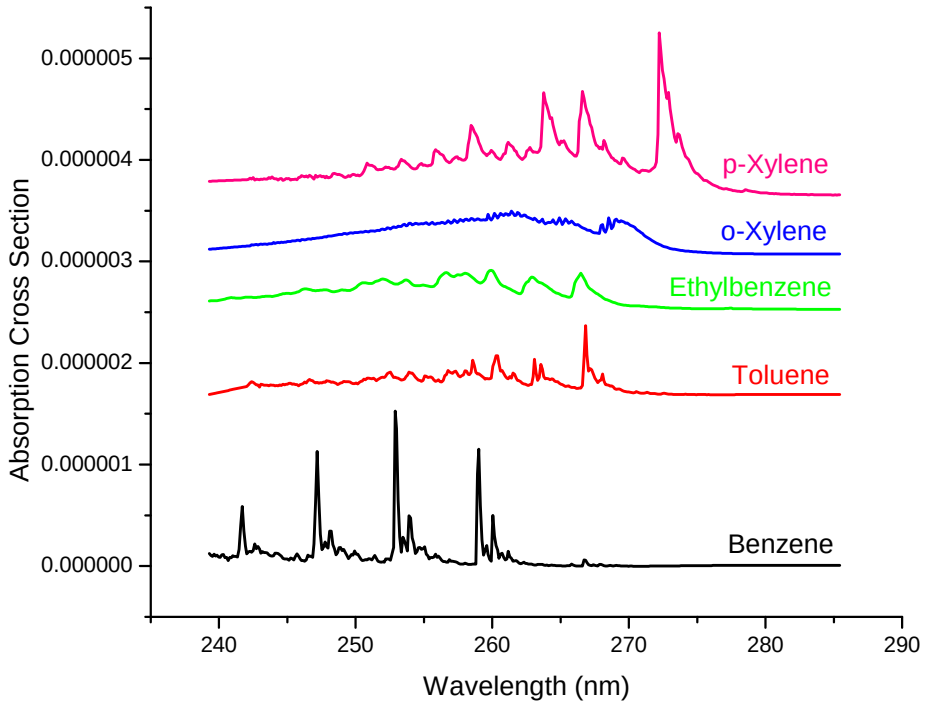

Fig. 2.19. Absorption cross sections of benzene, toluene, ethylbenzene, o-, and p-xylene in the UV region [72].

lengths were used in the five compound measurements as I improved the mid-IR system. The measurements were carried out twice using the 70 m path length setup, once with the 100 m path length setup, and three times in the last modified setup with 110 m path length. Results of each experiment will be discussed in detail in Chapter 3.

Chapter 3

Results & Discussion

In this chapter I will discuss the results of the experiments done during this study. These experiments consist of calibration measurements, preliminary measurements and final five compound measurements.

3.1 Calibration Measurement Results

As discussed in Chapter 2, both mid-IR and UV systems were calibrated for gas concentration measurements using a calibration gas generator. These calibration experiments were done under various conditions, including different sequences of calibration gases, and measurements while diluting and filling calibration gases to have a better understanding of the system and to provide more accurate results.

The resulting calibration curve for the UV system is shown in Fig. 3.1 [13]. In this graph, the concentrations determined from the UV data are plotted versus the actual concentrations. The UV data are shown as solid circles with the solid line as the best linear fit through them.

For the mid-IR measurements on the other hand, I have used three different multipass cell configurations with 70, 100 and 110 m path lengths and also two different setups, i.e. single detector and double detector setups. Consequently, the calibration measurements were done several times and the resulting calibration curves are given below.

The calibration results for the 70 m path length mid-IR setup are shown in Fig. 3.2. This graph shows the concentrations determined from the mid-IR data versus

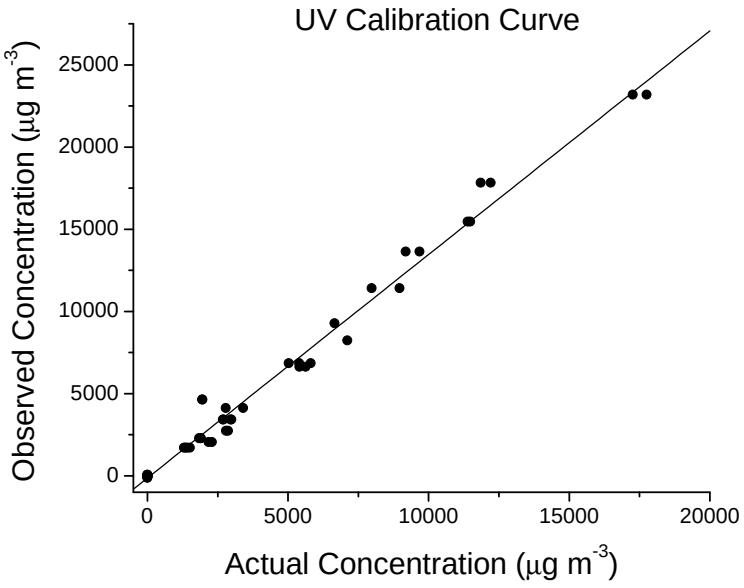

Fig. 3.1. UV calibration curve. The solid circles are the data extracted from the experimental results; the solid line is the best linear fit [13].

the actual concentrations. The open circles represent the mid-IR data with the solid line as their best linear fit. To obtain this graph, the mid-IR system was calibrated using three different gas concentrations: 1, 2 and 3 *ppm*.

Fig. 3.3 represents the calibration results for mid-IR system with 100 m path length. In this graph, the mid-IR data are shown as open circles and the solid line represents the best linear fit. Fig. 3.3 demonstrates that the performance of the mid-IR system improved in going from 70 m to 100 m path length. The slope of the linear fit through this data set is closer to 1 than the slope of the linear fit through the previous data set. Also, the y-axis intercept is closer to zero. This is a good improvement toward the goal to detect gas concentrations as close as possible to the actual concentrations as provided by the Kin-Tek calibration gas generator. The system was calibrated using gas concentrations in the range from 0.5 *ppm* to 4 *ppm*. Both 70 m and 100 m path length setups were used in single mid-IR detector configuration (single detector setup).

The calibration curve for the mid-IR system in two detectors and 110 m path length configuration is shown in Fig. 3.4.

The mid-IR data are represented by solid circles. Each point in this graph rep-

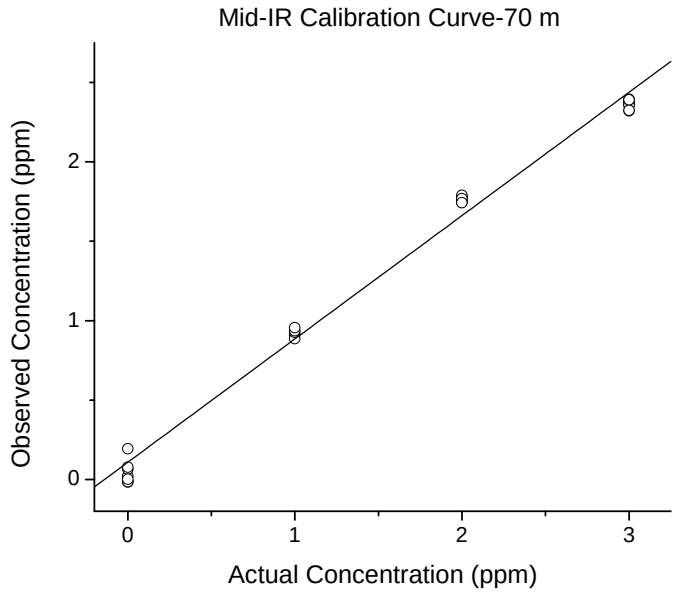

Fig. 3.2. Mid-IR calibration curve obtained from measurements with the 70 m path length/single detector setup. The open circles are the data extracted from the experimental results; the solid line is the best linear fit to the data.

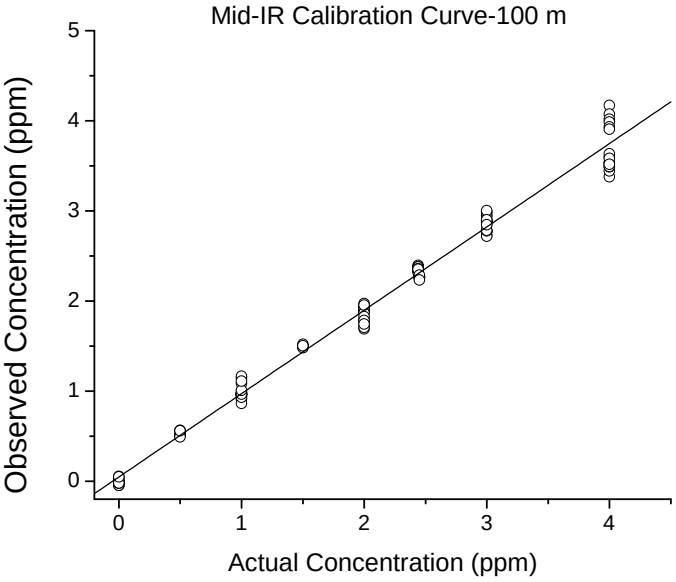

Fig. 3.3. Mid-IR calibration curve obtained using the 100 m path length/single detector setup. The open circles represent the data extracted from the experimental spectra; the solid line is the best fit.

resents an average over 10 data points. The solid line is the best linear fit through them. As shown in Fig. 3.4, gas concentrations were measured in a wider range, i.e.

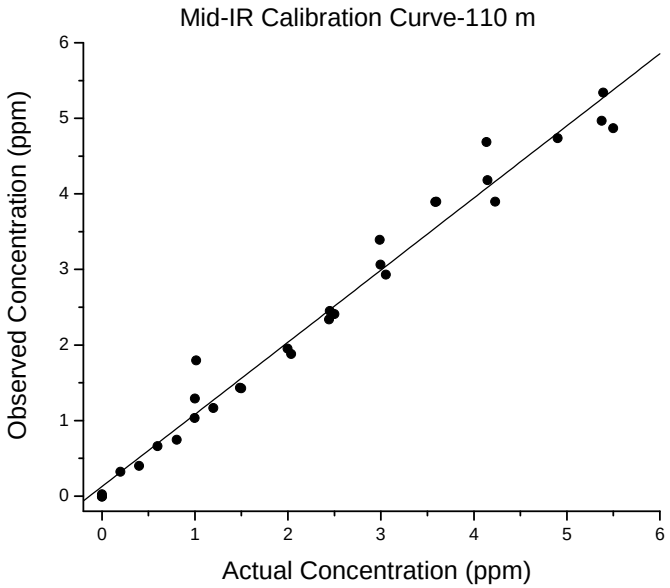

Fig. 3.4. Mid-IR calibration curve in the 110 m path length/double detector setup. Solid circles are data, solid line is the best fit.

from 0 *ppm* to 5.6 *ppm*. The interesting point is, that it was possible to detect lower concentrations, as low as 0.2 *ppm* (the detection limit for p-xylene in the 70 m path length setup) with an acceptable amount of noise. Reducing the noise level in the system was the main goal of this system modification from single detector to double detector setup.

Table 3.1 [13] shows specifications of the mid-IR system before any modifications were done, together with those of the UV system.

The detection limit is "the lowest concentration level that can be determined to

	Mid-IR			UV		
Compound	Detection Limit (ppb)	Limit of Quantitation (ppb)	Uncertainty (ppb)	Detection Limit (ppb)	Limit of Quantitation (ppb)	Uncertainty (ppb)
Benzene	60	200	200	20	70	60
Toluene	70	200	200	40	100	50
p-Xylene	200	600	200	10	30	40
Path Length (m)		70			1.2	
Full Wavelength Range		9.41–9.88 μm (1012–1063 cm^{-1})			215–400 nm	
Resolution		0.002 cm^{-1}			0.118 nm	
Scans Averaged		10			5000	
Scan Rate (min^{-1})		2			1500	

TABLE 3.1
Specifications of, and performance comparison between, UV and mid-IR systems (70 m path length) [13].

be statically different from a blank" with 99% confidence [73]. The detection limits for each gas measured with the mid-IR and UV systems are calculated using Eq. 3.1 [74].

$$\text{Detection Limit of gas } i = \frac{3 * s_i}{m} \tag{3.1}$$

Here s_i is the standard deviation of the observed background concentration of gas i in a blank sample, and m is the slope of the calibration curve.

The limit of quantitation is "the level above which quantitive results may be obtained with a specific degree of confidence" [73]. Similarly, we calculated the limits of quantitation using Eq. 3.2 [74].

$$\text{Limit of Quantitation of gas } i = \frac{10 * s_i}{m} \tag{3.2}$$

The uncertainty of a measurement is "the doubt about the results of the measurement", so it tells us something about the "quality of the measurement" [75]. In other words, uncertainty is "a quantification of the doubt about the measurement results" [75]. We have used three times the standard deviation of the observed background concentrations as the estimated uncertainty [76].

The reason for using these concepts here is to assess the performances of the UV and mid-IR systems quantitively and also to be able to compare them. It can be noticed from Table 3.1 [13], that detection limit, limit of quantitation and also uncertainty for benzene, toluene and especially p-xylene are much lower for the UV system compared to the mid-IR system with 70 m path length. It should be mentioned that the number of spectra to be averaged is around 500 times more in the UV system which helps to reduce the uncertainty of the measurements and consequently the detection limits and limits of quantitation. Besides, p-xylene has a single weak peak in this mid-IR region whereas its strong features in the UV help to detect this gas better using the UV system.

As mentioned before, in order to improve the mid-IR system I increased the absorption path length (from 70 m to 110 m) and also implemented the two detector setup. The Table 3.2 shows the specifications of the mid-IR system with 110 m path length after the recent improvements.

Mid-IR System	Benzene	Toluene	Ethylbenzene	o-Xylene	p-Xylene
Detection Limit (ppb)	59	72	62	66	62
Limit of Quantitation (ppb)	199	243	207	219	207
Uncertainty (ppb)	60	60	60	60	60

TABLE 3.2
Specifications of the mid-IR system with 110 m path length after the recent improvements.

When comparing the detection limit and limit of quantitation of p-xylene in mid-IR 70 m and 110 m systems, a substantial improvement can be noticed. For p-xylene which has a single weak peak in the mid-IR region of our interest, improving the system sensitivity and reducing the uncertainty through path length extension and implementing another detector in the mid-IR system, can help decreasing the detection limit and also the limit of quantitation of this gas in the mid-IR system, more significantly compared to benzene and toluene.

3.2 Results from the Preliminary Experiments

As discussed before, I have done a series of preliminary experiments with o-xylene and ethylbenzene to check the possibility of detecting these two gases with the UV and mid-IR systems. In this part I will discuss the resulting graphs.

3.2.1 Single Compound Measurements

Fig. 3.5 represents the measurement results of the first single compound experiment in which the reaction of o-xylene with hydroxyl radicals was monitored inside the photoreaction chamber.

In this graph, the o-xylene concentrations are plotted as a percentage of its initial concentration versus the reaction time in minutes. The initial concentration of o-xylene was determined to be about 0.6 ppm using the mid-IR system. UV data are shown as filled black symbols, while mid-IR data are represented by filled gray symbols. Data shown in this plot were calibrated. As expected, the concentration of o-xylene decreases as the reaction proceeds. The error bars shown in these graphs, are the percentage ratio of the uncertainty to the concentration of the gas at that specific time.

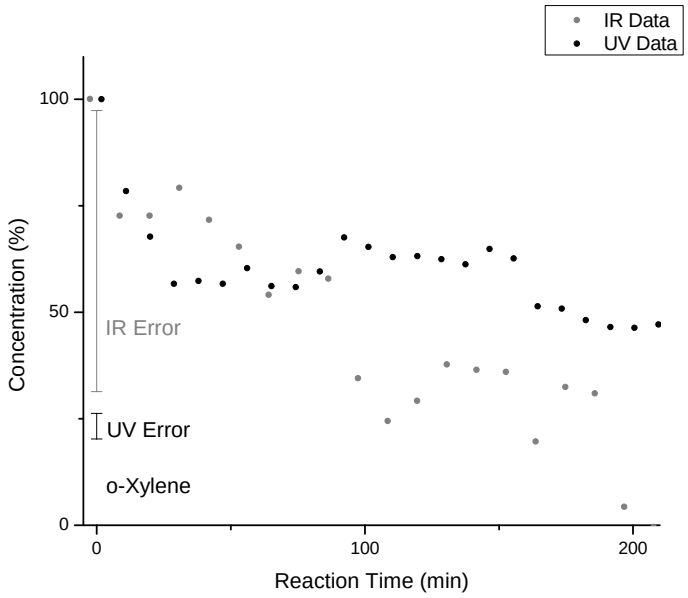

Fig. 3.5. o-xylene gas concentration as a function of time in the first o-xylene measurement.

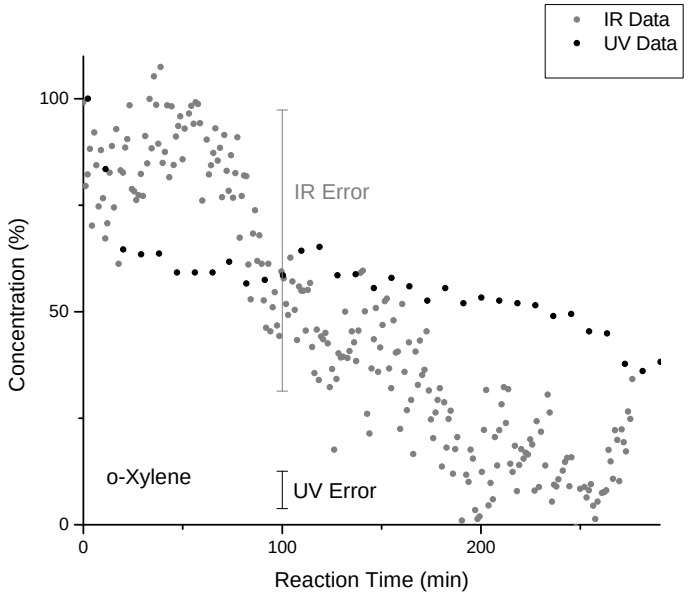

Fig. 3.6. o-xylene gas concentration as a function of time in the second o-xylene measurement.

Fig. 3.6 represents a second experiment with identical conditions except for the initial concentration of o-xylene which was detected to be about 1.03 *ppm* using the mid-IR system. As seen in this graph, there is much less noise in the UV data compared to the mid-IR data. One reason is that each data point from the UV

data is the result of averaging 10000 UV spectra, while only 10 mid-IR spectra were averaged in these measurements. Consequently, detection limit and uncertainty for o-xylene measurements are lower in the UV system compared to the mid-IR system.

In addition, each gas has a different spectrum in the UV and mid-IR regions, which sometimes makes the detection easier in one region rather than the other. I am comparing the mid-IR results with the UV results to have data confirmation. It should be mentioned that measurement errors increase as gas concentrations decrease over time. The gas concentrations may even go below the detection limit at some point.

Fig. 3.7 shows the results of the third single compound measurements in which the reaction of only ethylbenzene with hydroxyl radicals was monitored inside the photoreaction chamber.

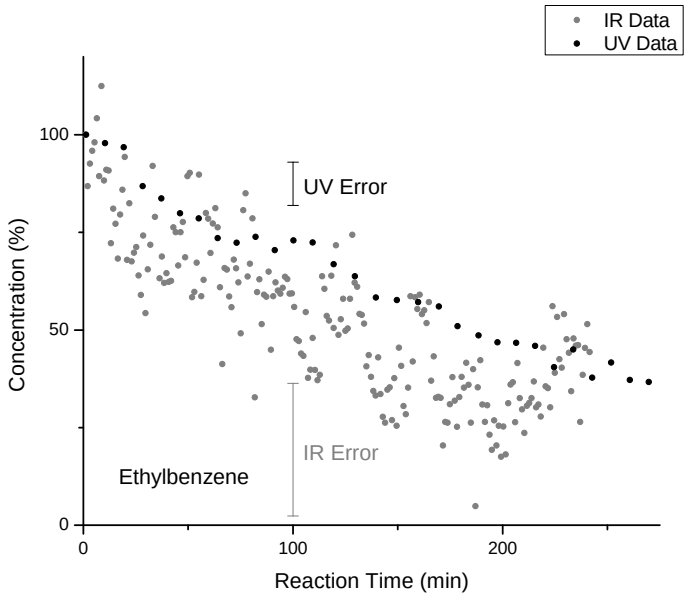

Fig. 3.7. Ethylbenzene gas concentration as a function of time in the first ethylbenzene measurement.

This graph shows the decrease in the ethylbenzene concentrations over reaction time as a percentage of its initial concentration. The initial concentration of ethylbenzene in this test was determined to be about 2.2 *ppm* using the mid-IR system. UV data are shown as filled black symbols, while mid-IR data are represented by filled gray symbols. The data shown in this plot were also calibrated. An exponen-

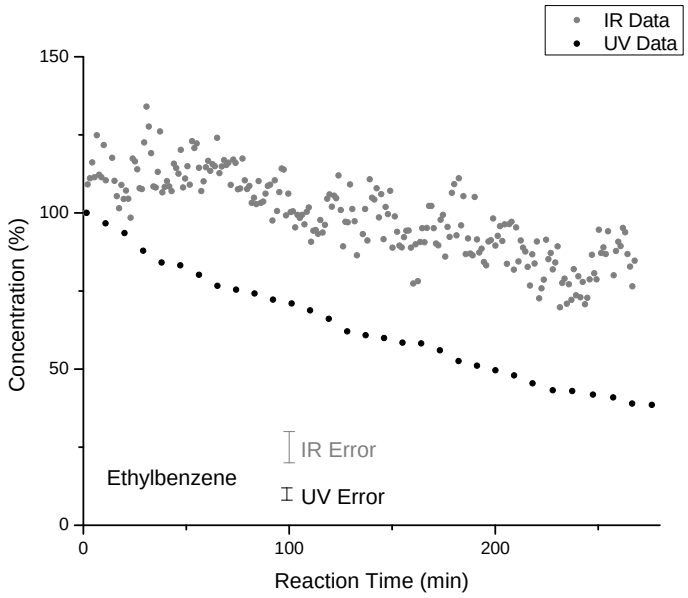

Fig. 3.8. Ethylbenzene gas concentration as a function of time in the second ethylbenzene measurement.

tial decay in the ethylbenzene concentrations can be seen in this data. The UV and mid-IR results are in reasonable agreement considering the noise in the mid-IR data. This is a step forward in reaching the goal of being able to detect additional, and perhaps multiple, gases using the system.

Fig. 3.8 represents a second measurement with ethylbenzene. The test conditions were the same as the previous time except for the initial concentration of ethylbenzene which was determined to be about 3.6 *ppm* using the mid-IR system. Although the initial concentration is higher in this experiment compared to the previous one, it displays more noise in the mid-IR data. On the other hand, the UV data are showing an exponential decay in gas concentrations, as expected, and the noise level is low. Again here, the relative measurement errors increase as gas concentrations decrease over time specially for the mid-IR data.

3.2.2 Double Compound Measurements

In this set of experiments, I measured concentrations of both ethylbenzene and o-xylene in the photoreaction chamber. The objective of these measurements was to see if it is possible to detect these two gases together using UV and mid-IR systems.

Fig. 3.9 shows the results of the first double compound experiment. In this graph, o-xylene and ethylbenzene concentrations are plotted as a percentage of their initial concentration versus the reaction time. The initial concentration of o-xylene in this test was determined to be about 1.01 *ppm* using the mid-IR system, while the initial concentration of ethylbenzene was determined to be about 1.05 *ppm*. UV data are shown as filled black symbols and mid-IR data are represented by filled gray symbols. I calibrated the data shown in this plot. As expected, the concentration of ethylbenzene decreases as it undergoes the reaction. The noise level in the mid-IR ethylbenzene data is higher than in the UV ethylbenzene data. As the reaction time increases, the gas concentrations decrease and make the detection even harder specifically in the mid-IR system which has higher detection limits.

Fig. 3.10 shows results from a second test with exactly same conditions as before, except for the initial concentrations of ethylbenzene and o-xylene which were 1.7 *ppm* and 1.6 *ppm*, respectively as determined using the mid-IR system. As shown in this figure, there is less noise in the o-xylene data compared to Fig. 3.9. The reasons for ethylbenzene to look noisy are its weak absorptions in the UV and mid-IR range.

3.3 Results from Five Compound Measurements

Finally I studied a mixture of all five compounds (benzene, toluene, ethylbenzene, o-xylene and p-xylene) in the photoreaction chamber to see if I am still able to detect them individually. Separate experiments were previously done, monitoring the reaction of these gases with putting only one, two (i.e. ethylbenzene + o-xylene, or benzene + p-xylene [13]), or three (i.e. benzene + toluene + p-xylene [13]) of them in the photoreaction chamber.

Results of the first experiment with all five compounds are shown in Fig. 3.11. This graph shows the spectroscopic measurements of BTEX gas concentrations using both mid-IR and UV systems as function of the reaction time. UV data are shown as black filled circles, while mid-IR data are represented by the filled gray symbols.

The initial concentrations of benzene, toluene, ethylbenzene, o-, and p-xylene measured by using the mid-IR system were 2.4, 2.8, 5.4, 2.9, 4.6 *ppm*, respectively. Fig. 3.11 shows the measured gas concentrations as a percentage of the initial con-

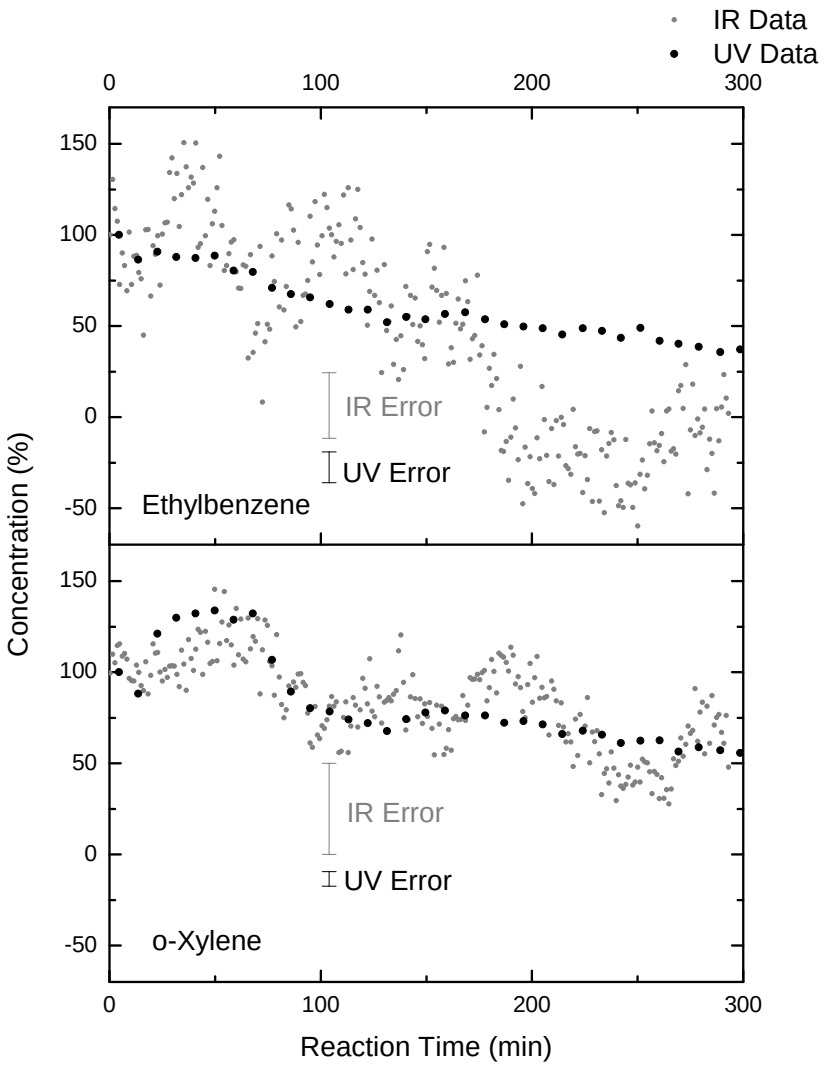

Fig. 3.9. Ethylbenzene and o-xylene gas concentrations as a function of time.

centration of each gas after calibration.

There is good agreement between determined benzene concentrations from the mid-IR and the UV data, when looking at percentages. For toluene and ethylbenzene the mid-IR and UV data show moderate agreement. We note that toluene and ethylbenzene peaks overlap at around 1032 cm^{-1} in the mid-IR region. At some regions in Fig. 3.11 we can see that the concentrations are measured higher for toluene and lower for ethylbenzene and vice versa in other regions. For o-xylene and p-xylene concentration measurements, there are some mismatches between the UV and mid-IR results due to interferences between their peaks in the mid-IR region at approximately 1024 cm^{-1}. Additionally, ethylbenzene and p-xylene also exhibit

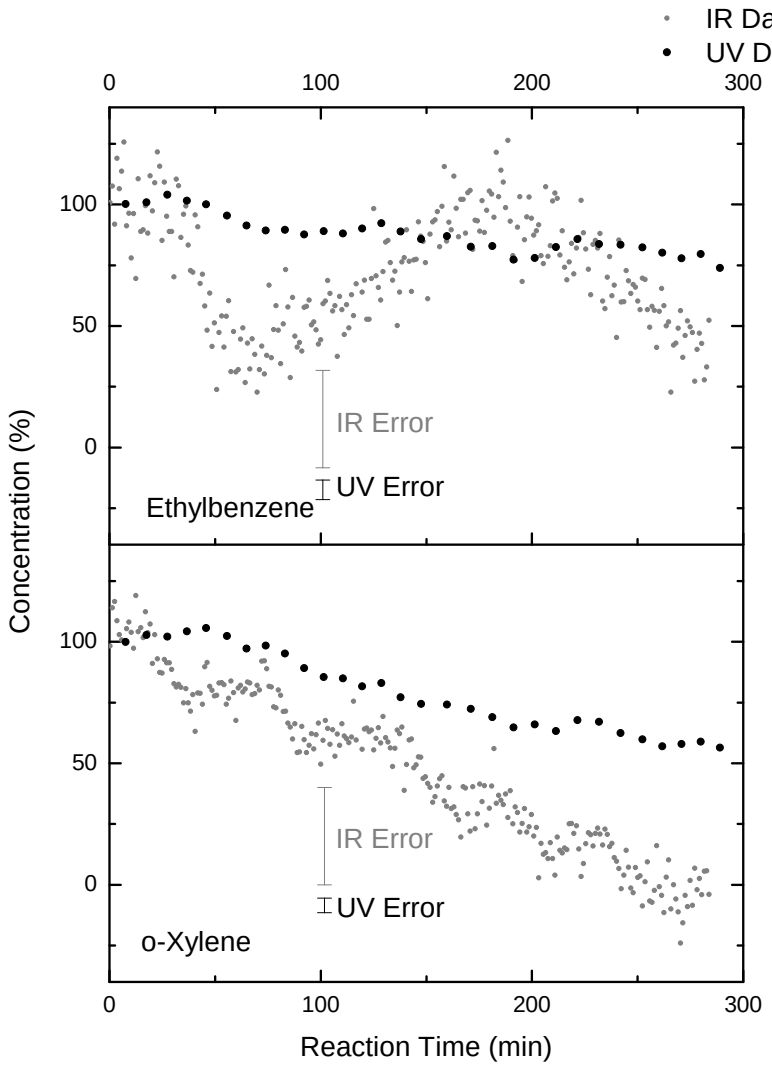

Fig. 3.10. Ethylbenzene and o-xylene gas concentrations as a function of time.

rather weak absorption features in the mid-IR range of this particular EC-QCL, which results in significant uncertainty in measuring their concentrations with the EC-QCL used in this study.

Results for the second five compound measurements are shown in Fig. 3.12. The BTEX gas concentrations determined using both mid-IR and UV systems over the reaction time are shown in this graph. UV data are shown as hollow circles, while mid-IR data are represented by black symbols. Sample error bars at 130 minutes of the reaction are also shown in this graph. These error bars are smaller for the UV data compared to the mid-IR data. Among the mid-IR data, ethylbenzene has the largest error bar at 130 *min*.

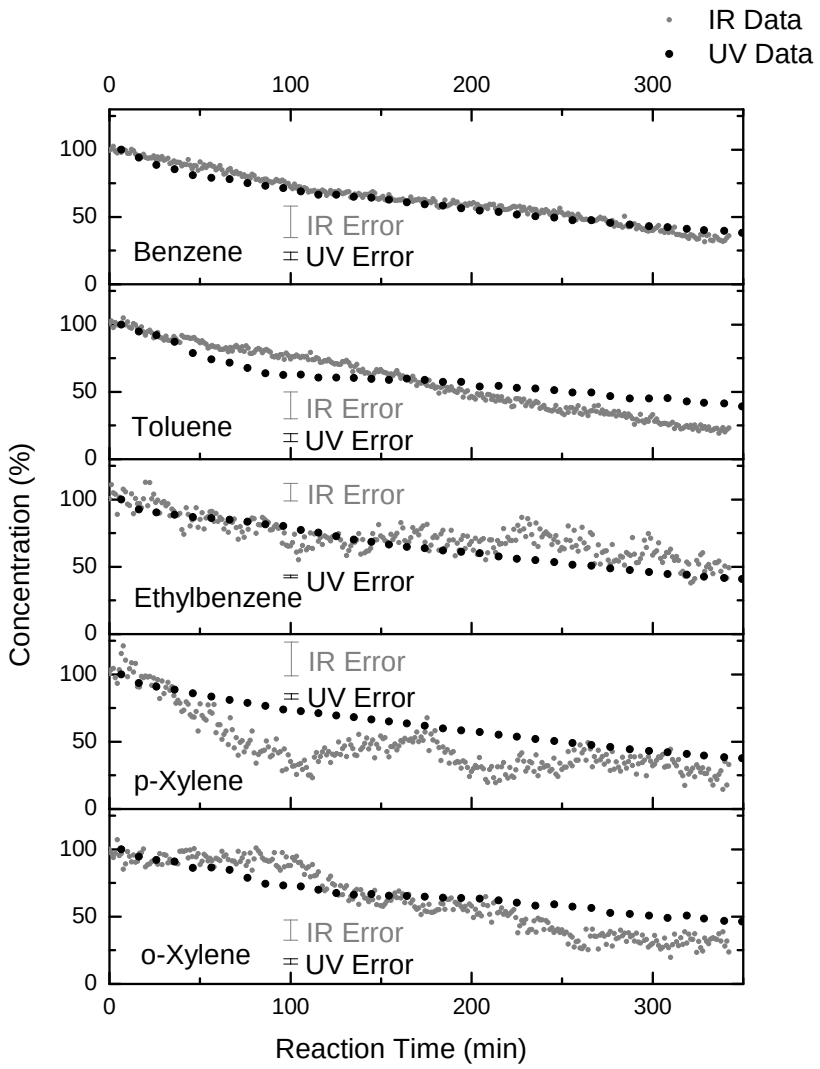

Fig. 3.11. Benzene, toluene, ethylbenzene, o- and p-xylene gas concentrations as a function of time; first five compound measurement using the 70 m path length mid-IR system. UV data are shown as black filled circles, while mid-IR data are represented by the filled gray symbols.

The initial concentrations of benzene, toluene, ethylbenzene, o-, and p-xylene, as measured by the mid-IR system were 2.6, 3.03, 3.2, 4.9, and 5.1 ppm, respectively. In Fig. 3.12, the measured gas concentrations are shown as a percentage of the initial concentration of each gas after calibration.

Again, there is good agreement between benzene concentrations from mid-IR and UV data. For toluene, the mid-IR and UV data show some discrepancies. The ethylbenzene data have more noise in the mid-IR data than the UV data. o-xylene and p-xylene percentage concentrations from the mid-IR data, are in better agreement with the UV results compared to the previous measurements. There is

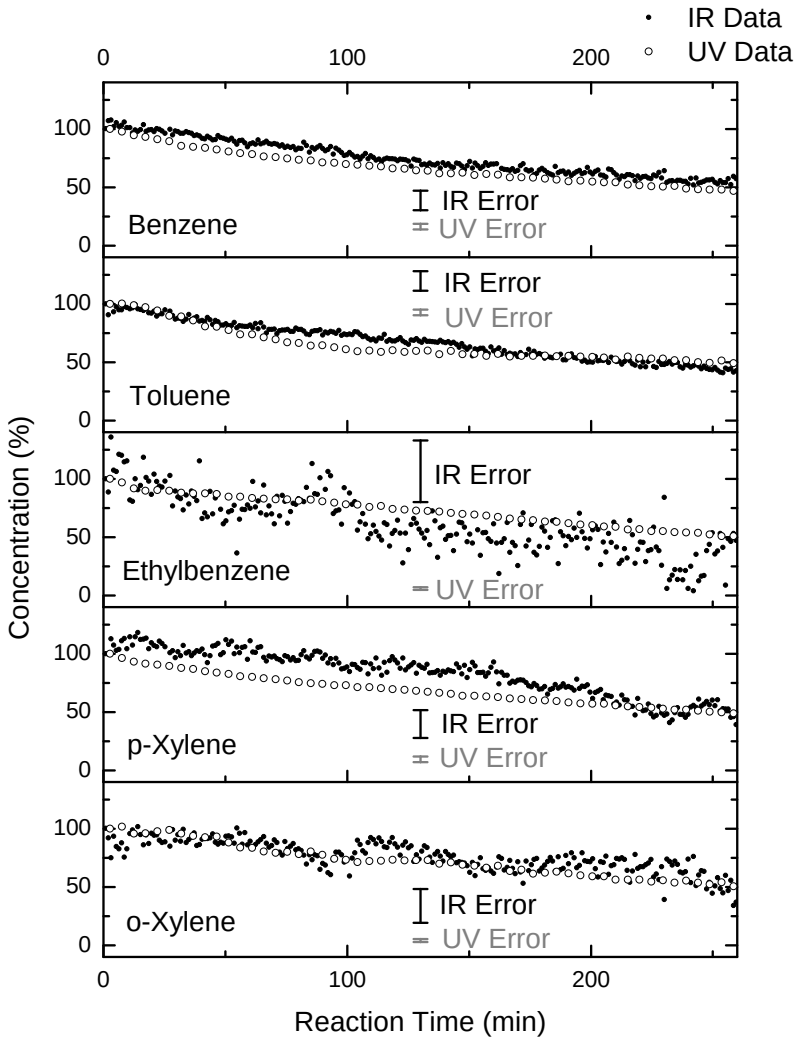

Fig. 3.12. Benzene, toluene, ethylbenzene, o- and p-xylene gas concentrations as a function of time; second five compound measurement using the 70 m path length mid-IR system. UV data are shown as hollow circles, while mid-IR data are represented by black symbols.

still more noise in the mid-IR data than the UV for these compounds, which leaves room for improvement.

The five compound measurement results discussed above were done with the 70 m path length mid-IR system configuration. The five compound measurement results obtained with the 100 m path length mid-IR system configuration are shown in Fig. 3.13. This graph shows the BTEX gas concentrations determined from both mid-IR and UV measurements as function of reaction time. UV data are shown as gray filled circles, while mid-IR data are represented by black filled symbols.

The initial concentrations of benzene, toluene, ethylbenzene, p-xylene, and o-

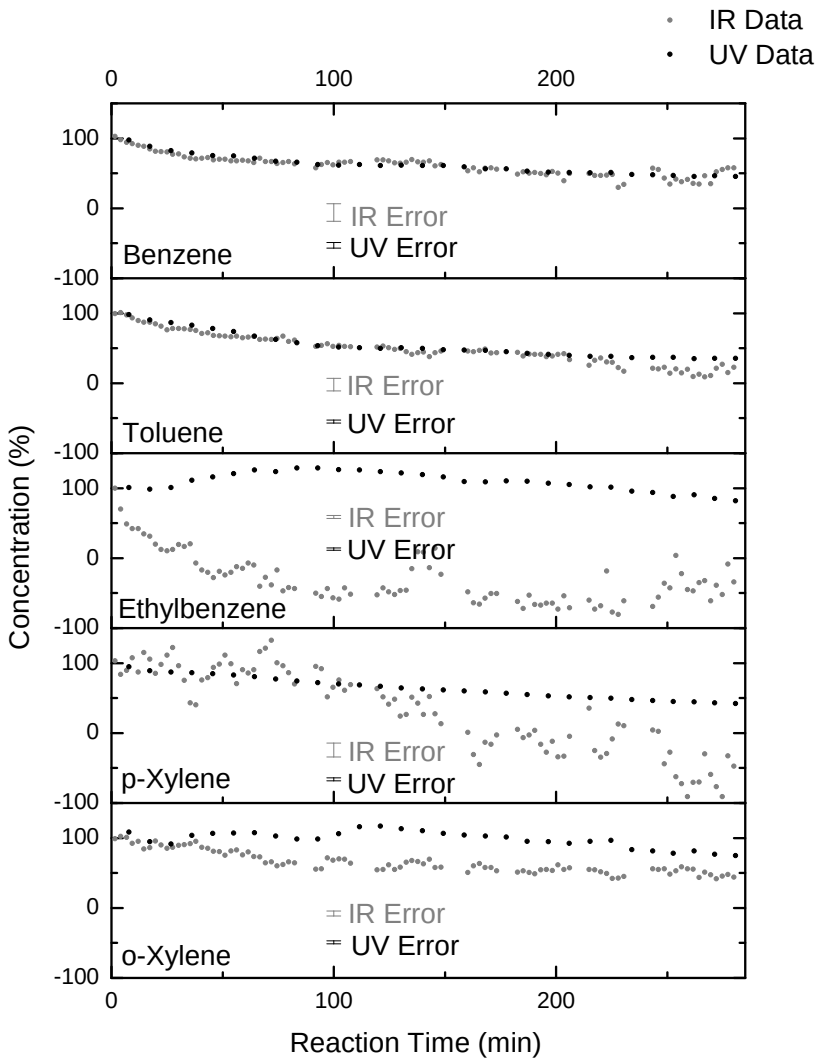

Fig. 3.13. Benzene, toluene, ethylbenzene, o- and p-xylene gas concentrations as a function of time; third five compound measurement using the 100 m path length mid-IR system. UV data are shown as black filled circles, while mid-IR data are represented by gray filled circles.

xylene in this test measured with the mid-IR system were 1.3, 2.1, -7.9, 1.5, and 4.2 *ppm*, respectively. Fig. 3.13 shows the determined gas concentrations as a percentage of the initial concentration of each gas after calibration.

There is a good agreement in percentage concentrations between benzene and toluene concentrations measurements in mid-IR and UV systems. There appears to be a problem with the ethylbenzene data from this experiment, as its initial concentration was measured to be around -8 *ppm* using the mid-IR system. That could be the reason why the ethylbenzene concentrations determined from the mid-IR data do not match with UV data. In case of the o-xylene and p-xylene concentration

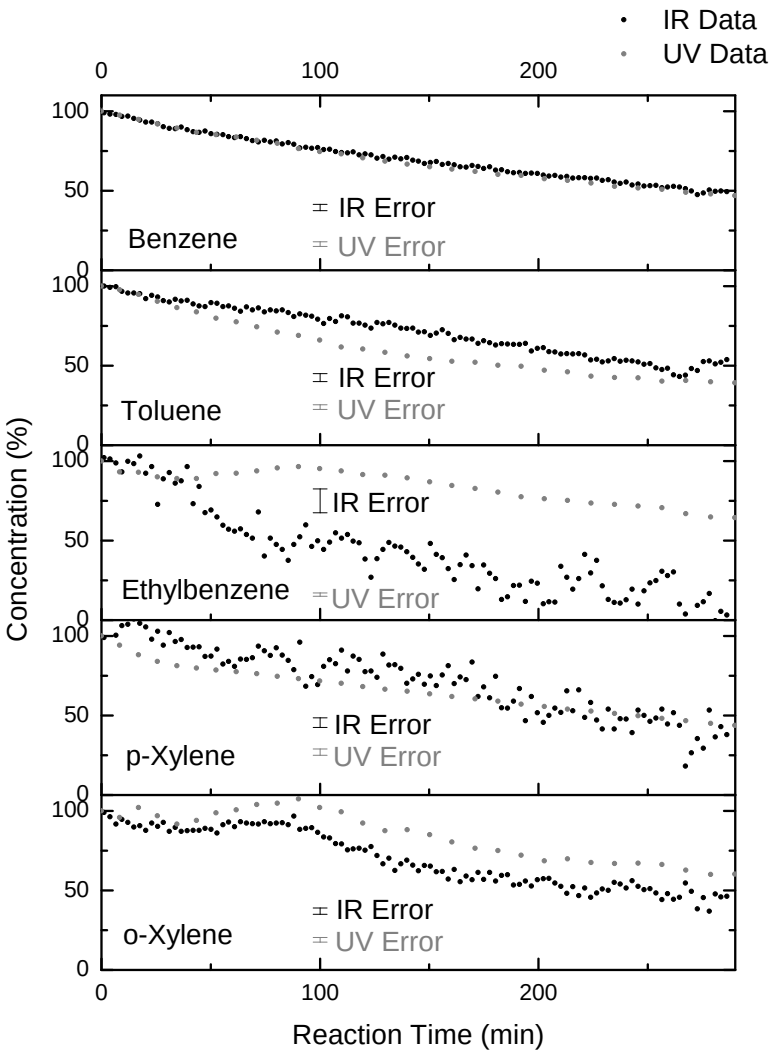

Fig. 3.14. Benzene, toluene, ethylbenzene, o- and p-xylene gas concentrations as a function of time; fourth five compound measurement using the 100 m path length mid-IR system. UV data are shown as gray filled circles, while mid-IR data are represented by black filled symbols.

measurements, there are some mismatches between the UV and mid-IR results. This is a result of interferences between their peaks in mid-IR region at approximately 1024 cm^{-1}.

The negative concentrations obtained for ethylbenzene in this measurement wants some discussion: First of all, ethylbenzene has only a rather weak absorption feature at about 1031 cm^{-1} in the region of interest (see Fig. 2.18). In addition there is significant overlaps between ethylbenzene and toluene peaks. This makes it challenging to detect this gas and measure its concentrations in this region. This is compounded by the occurrence of fringes in the laser signal, which are caused by the etalon effects

due to the presence of a number of optical reflective surfaces (beam splitter, lens, window, for example). I attempted to reduce these fringes through smoothing the laser output spectrum by applying a low pass filter with cut off frequency of 20 Hz but this way we are actually losing some data. However, this also resulted in loss of information about the ethylbenzene concentration.

Another factor was the variation of laser output power during the measurement and even from scan to scan. These fluctuations can not be properly accounted for in these initial experiments, where only a single reference spectrum was recorded.

The above mentioned issue can then have significant correspondence when calculating the differential optical absorption spectrum, such as negative concentrations.

It should be mentioned that, despite some of the mismatches between mid-IR and UV data, there appears to be less noise in the mid-IR data compared to the previous experiments. This is a step forward in improving our mid-IR system. Further improvements were made by increasing the path length to 110 m and by including a second detector for simultaneous measurements of reference spectra.

The next five compound measurement was done using the double detector, 110 m path length mid-IR system configuration; both UV and mid-IR results are shown in Fig. 3.14. The initial concentrations of benzene, toluene, ethylbenzene, o-, and p-xylene measured with the mid-IR system were 3.7, 3.1, 1.7, 3.7 and 2.4 ppm, respectively. In Fig. 3.14, the measured gas concentrations are shown as a percentage of the initial concentration of each gas after calibration.

Fig. 3.14 shows that the o-xylene concentrations from mid-IR and UV measurements are in a good agreement. For p-xylene, the mid-IR data seem to be noisy compared to the UV data. The reason is the overlap between p-xylene and o-xylene features in the mid-IR region. Also in this graph, one can see that the concentrations are higher for toluene and lower for ethylbenzene in some regions and vice versa in others. The reason is the overlap of toluene and ethylbenzene peaks at around 1032 cm^{-1} in the mid-IR region. It appears that the double detector setup in the mid-IR system has led to significantly improved data, as we do not see any negative numbers for the ethylbenzene in these measurement results.

Fig. 3.15 shows the results of the next five compound experiment which was done using the double detector, 110 m path length mid-IR system. This graph shows

the BTEX gas concentration measurements from both mid-IR and UV systems as a percentage of the initial concentration of each gas as function of the reaction time. UV and mid-IR data are shown as gray and black filled symbols, respectively. The determined gas concentrations shown in Fig. 3.15 are calibrated. The initial concentrations of benzene, toluene, ethylbenzene, o-, and p-xylene as measured by the mid-IR system were 1.8, 2.2, 1.6, 3.1 and 2.5 *ppm*, respectively.

There is a good agreement between benzene percentage concentrations from the mid-IR and UV measurements. The p-xylene percentage concentrations from the mid-IR system also match with the UV data; there is only minor noise in the mid-IR data which make them fluctuate around UV data. For o-xylene, the mid-IR data have less noise compared to the previous measurement which had the same conditions as this test except for the initial concentrations. As mentioned before, the toluene and ethylbenzene peaks overlap in the mid-IR range. In some regions in the graph the concentrations are measured higher for toluene and lower for ethylbenzene and vice versa in others. Toluene concentrations from the mid-IR system are following the UV measurements but do not exactly match them. The ethylbenzene concentrations from the UV measurements show the greater discrepancy to the IR data.

The last five compound measurement results are shown in Fig. 3.16. These measurements were also done using the double detector, 110 m path length mid-IR system. The graph shows the gas concentrations measured with both UV and mid-IR systems, as a function of time. Concentrations shown in Fig. 3.16 are plotted as a percentage of the initial concentration of each gas over the reaction time after calibration. UV data are shown as gray filled symbols, while mid-IR data are represented by hollow black circles. The initial concentrations of benzene, toluene, ethylbenzene, o-, and p-xylene measured with the mid-IR system were 3.01, 3.9, 6.06, 8.7 and 3.2 *ppm*, respectively.

There is a good agreement between benzene percentage concentrations measured using the mid-IR and UV systems. o-xylene percentage concentrations from the mid-IR system match very well with the UV data during the first 100 minutes of reaction. After that, there are some mismatches between mid-IR and UV measurements. For p-xylene, the mid-IR data appear to have more noise compared to the data from previous measurements shown in Fig. 3.15, which was done under the

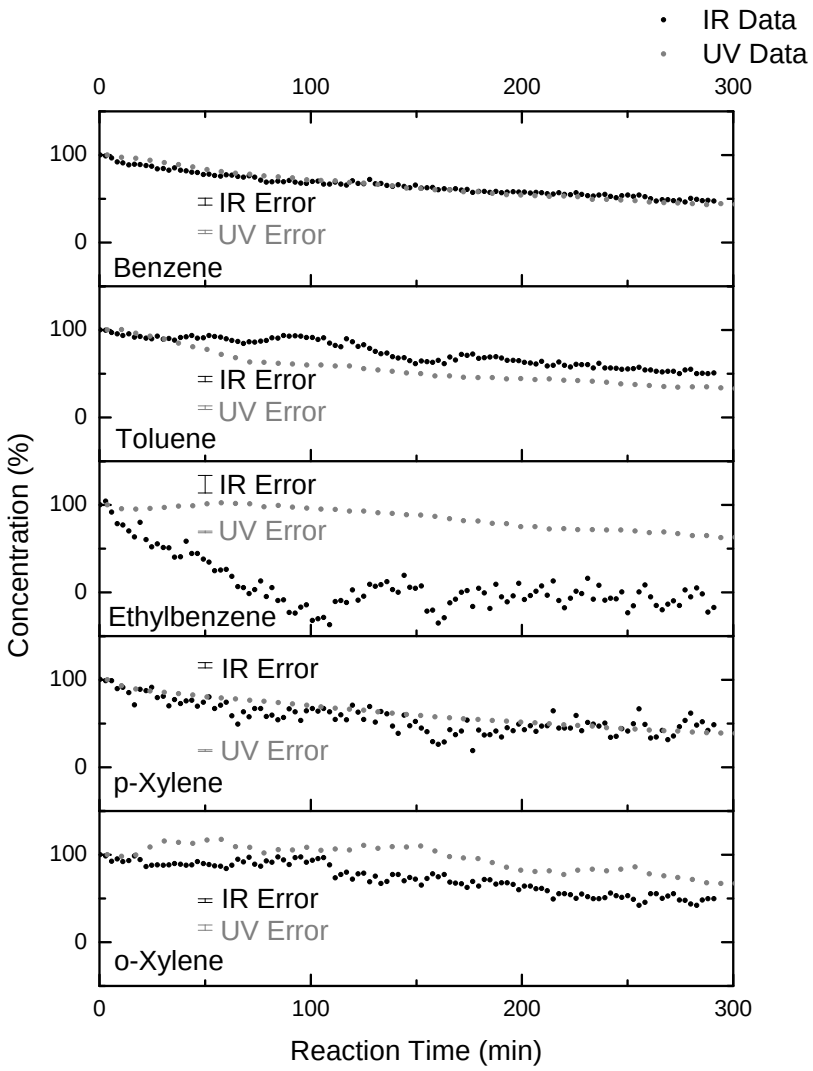

Fig. 3.15. Benzene, toluene, ethylbenzene, o- and p-xylene gas concentrations as a function of time; fifth trial using the double detector 110 m path length mid-IR system. UV and mid-IR data are shown as gray and black filled symbols, respectively.

same conditions as this experiment except for the initial concentrations. The UV data for p-xylene show a decrease in gas concentrations as expected. In the toluene and ethylbenzene concentration measurements there are still problems resulting from the interferences between their spectroscopic signature in the mid-IR region. After a short initial period of about 20 min, the ethylbenzene concentrations are too high and the toluene concentrations are low. The ratio of the discrepancies for ethylbenzene and toluene is between 1:3 and 1:4, similar to the ratio of the respective peaks in the mid-IR spectra (Fig. 2.18).

The reason we are comparing our mid-IR data with UV data is that as discussed

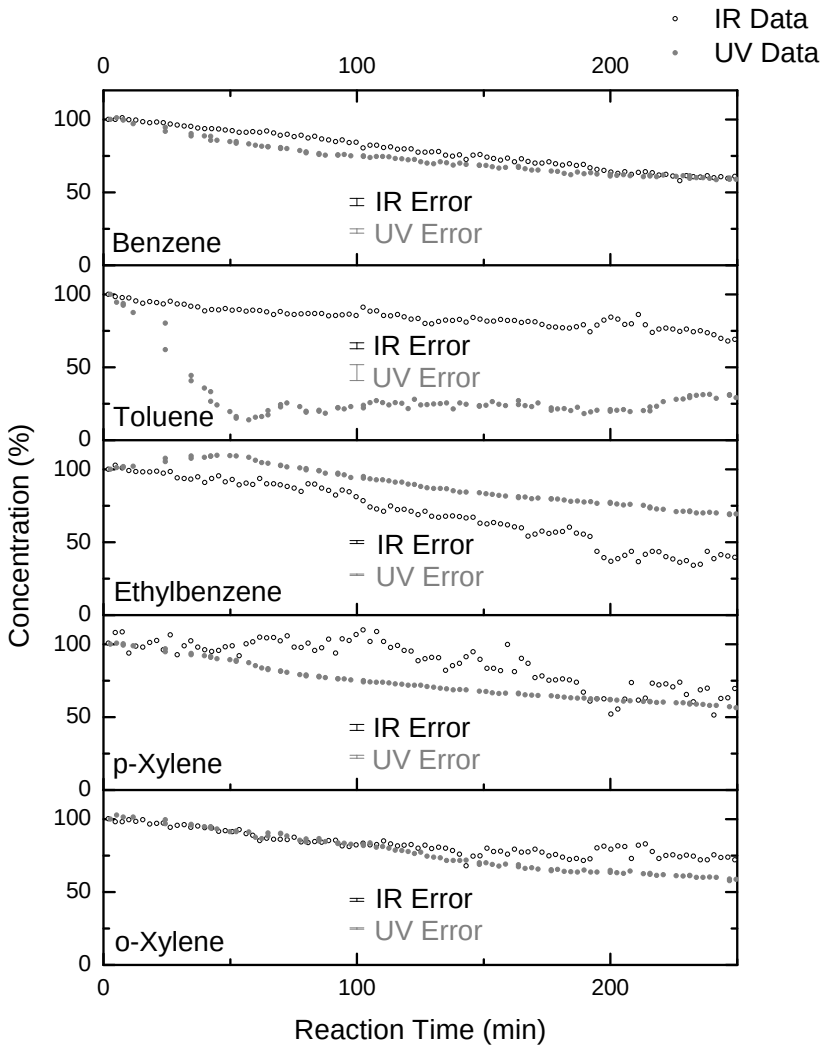

Fig. 3.16. Benzene, toluene, ethylbenzene, o- and p-xylene gas concentrations as a function of time; last five compound test using the double detector 110 m path length mid-IR system. UV data are shown as gray filled symbols, while mid-IR data are represented by hollow black circles.

earlier, UV DOAS is a proven method to study BTEX gases [42] because they have distinct absorption peaks in this region (220-290 nm). The UV spectrometer is a commercial system which allows fast averaging of around 15000 spectra in around 100 *sec*. This leads to a significant reduction in noise and increases the accuracy of the measurements (see Table 3.1).

Regarding the percentage error bars included in the graphs representing the measurement results from mid-IR and UV data, it should be mentioned that each data point in mid-IR system represents an average of 10-30 mid-IR spectra, whereas 15000 UV spectra were averaged in order to obtain a single data point from the UV

system. On the other hand, more IR data points were taken per time interval than UV data. Binning of the IR data over a certain time frame would reduce the error in the IR data.

Our experimental results have shown secondary organic aerosol particle formation (see Fig. 3.17) which is dependent on both the presence of H_2O_2 and at least one BTEX gas in the photoreaction chamber irradiated with the UV black lights. We have observed that as the gas concentrations decrease during chemical reactions of BTEX gases, particles are formed. Using a condensation particle counter (CPC) we were able to measure the number of particles and their size. The particle number shows initially an increase and then a gradual decrease. The initial increase in the number of particles indicates that BTEX gases go through chemical transformation in the presence of UV light, and produce aerosol particles. According to our measurements, most of the particle sizes are in the range of 50-400 nm. There are several reasons for the subsequent decrease in the particle numbers in the photoreaction chamber, including particle coagulation, settling on the walls, and other losses. We have noticed that the diameter of the aerosol particles increase over time. This can be explained in that small particles may join together to produce larger particles or these small particles served as nuclei for growth of larger particles in condensation processes.

As we have particles inside the photoreaction chamber and also the mid-IR multipass cell, it is useful to consider their scattering effects on the UV and mid-IR beams. As described earlier, in our experiments we are using a mid-IR laser system with wavelength range from 9.41-9.88 μm and a UV lamp with wavelength range of 215-400 nm. As benzene, toluene, ethyl-benzene and o-, and p-xylene gases (i.e., BTEX gases) react with hydrogen peroxide inside the simulation chamber, aerosol particles form which would later be transfered to the multipass cell. The particles which we are dealing with fall in the size range of 50-400 nm (we have obtained these data using a particle sizer). According to Mie and Rayleigh scattering theories, there should not be any significant scattering effects caused by these particles on the mid-IR laser beam as it travels through the multipass cell. On the other hand, as the particle sizes are comparable with the UV light wavelength, they may have more noticeable scattering effects on the UV beam.

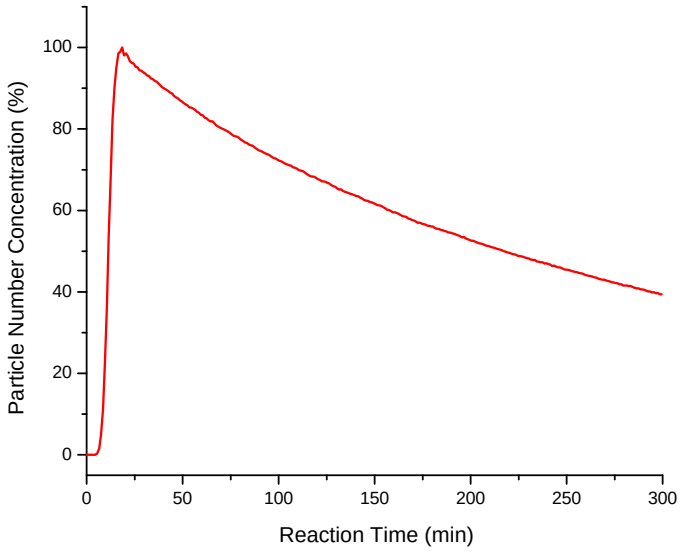

Fig. 3.17. Secondary organic aerosol particle formation inside the photoreaction chamber during chemical reactions of BTEX gases.

To show the effects of light scattering by aerosol particles on the mid-IR laser beam I have modeled this effect using MATLAB simulations.

As the diameter of the particles are much smaller than the wavelength of the laser light we are dealing with, Rayleigh equations are applied here. The refractive index of urban aerosol particles is $m = 1.56 - 0.087i$ [63]. The laser intensity inside the multipass cell is assumed to be 25 mW ($I_0 = 25\ mW$) at 9.6 μm. The intensity of the scattered light (I_s) is proportional to the intensity of the incident light (I_0). I_s is dependent on particle size, and the larger the particle diameter is the greater would be the scattering intensity (I_s). I have picked an average particle size of 200 nm for these simulations.

The simulation results showing the intensity of the scattered light in a polar diagram are shown in Fig. 3.18. Fig. 3.19 shows the simulation results for the ratio of I_s over I_0 as a function of scattering angle. By setting the scattering angle to zero to have maximum I_s, simulations give us the ratio of I_s to I_0 as a function of particle size, which is shown in Fig. 3.20.

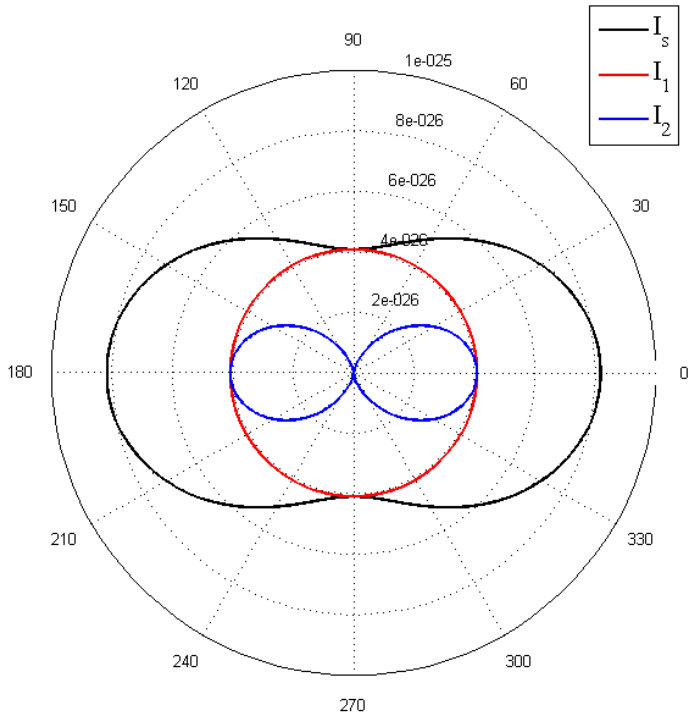

Fig. 3.18. Polar diagram of the scattered light.

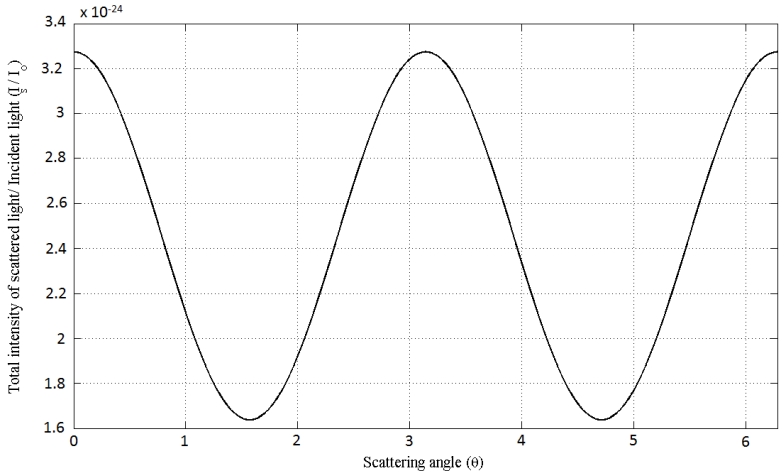

Fig. 3.19. Ratio of I_s to I_0 as a function of scattering angle.

As shown in the results of simulations, the maximum intensity of the scattered light in polar diagram at scattering angle of zero is $8.184 * 10^{-26}$, which is negligible. In Fig. 3.19, the ratio of the intensity of the scattered light (I_s) to the intensity of the incident light (I_0) as a function of scattering angle varies from $1.7 * 10^{-24} - 3.3 * 10^{-24}$

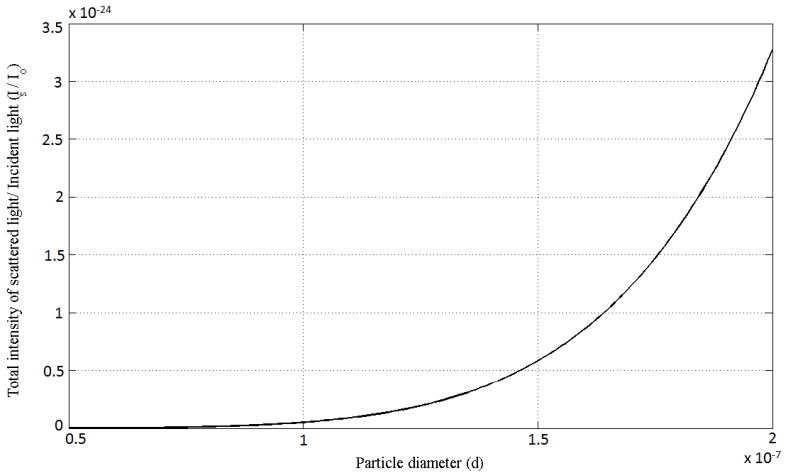

Fig. 3.20. Ratio of I_s to I_0 as a function of particle size.

which is negligible. And finally, the graph shown in Fig. 3.20, indicates the ratio of the intensity of the scattered light (I_s) to the intensity of the incident light (I_0) as a function of particle size. As expected, this ratio increases for larger particle diameters. Again, the small amount of $3.4 * 10^{-24}$ as its maximum shows that the intensity of scattered light is negligible. This means the effect of aerosol particles on the mid-IR laser beam is negligible.

In addition to secondary organic aerosol particle formation, we also observed the formation of a by-product in the reactions of hydroxyl radicals with BTEX compounds. Fig. 3.21 shows examples of mid-IR DOAS spectra for BTEX reactions at 0, 1, and 5 hours after initiation of the reaction. While the absorption lines of the BTEX gases decrease as the reaction goes on, there are several features that increase in amplitude with time. These features are marked with an arrow in Fig. 3.21. As these features have been noticed before specifically around 1033 cm^{-1} [13], with only benzene and toluene or benzene, toluene and p-xylene in the photoreaction chamber, we are confident that what we have measured is a by-product and that the features do not arise from system errors.

Our attempts to elucidate the source of this absorption features were unsuccessful (for either organic or inorganic compounds) and we label this feature as that of a by-product of the reactions. No corresponding absorption features from by-products were observed in the UV DOAS spectra during these experiments. Therefore, we emphasize the importance of using multiple monitoring methods such as mid-IR and

UV DOAS in measuring trace gas concentrations, either in the atmosphere or in simulated environments similar to the current study.

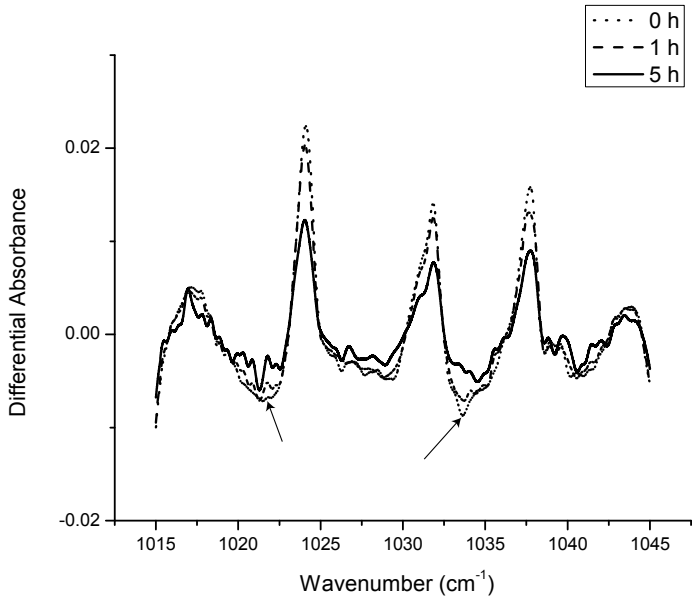

Fig. 3.21. Mid-IR DOAS spectra for BTEX reactions at 0, 1, and 5 hours of the reactions.

To sum up, for the BTEX concentration measurements in this study, I began with the investigation of two additional gases (ethylbenzene and o-xylene) and monitored their concentrations as they undergo reactions with hydroxyl radicals. Concentrations obtained from mid-IR data were found to be in agreement with UV data, within the respective uncertainties. There were some fluctuations observed in the mid-IR and even UV data. There can be a few reasons for this observation. First of all, I observed significant fringing effects with the IR beam as a result of etaloning between various optical surfaces (lenses, mirror, windows, beam splitters). Low pass filtering of the signal reduced the fringing effects, but also reduced the sensitivity of the spectrum. Furthermore, ethylbenzene and o-xylene have only weak absorption features in the IR and UV region, respectively. Additional difficulties come from the data manipulation to produce the DOAS spectra and the spectral fitting procedures. In addition, the second peak of o-xylene in the mid-IR region falls in the mode-hop region of the laser. Overall, it was successful monitoring these two new gases either individually or both together.

Subsequently, I let all five compounds react simultaneously in the photoreaction

chamber. Despite significant peak overlaps in the mid-IR region between ethylbenzene and toluene at 1032 cm^{-1} and o-xylene and p-xylene at 1024 cm^{-1}, it was possible to distinguish between these gases and monitor their concentrations in real-time as they react with hydroxyl radicals. The results from the mid-IR system were in agreement with the UV data within the uncertainty range. There were some discrepancies observed in the data which were mainly the result of overlaps between peaks in mid-IR region. It was noticed that the concentrations were determined higher for toluene and lower for ethylbenzene in some regions and vise versa. This was the case for o-xylene and p-xylene as well. The ratio of the difference between mid-IR and UV determined concentrations for these two pairs of gases is similar to the ratio of the peaks of these gases in mid-IR and UV regions, thus confirming that peak overlap leads to those variations.

After completing two measurements using this mid-IR system with 70 m path length, I increased the path length from 70 m to 100 m. With this improvement in the mid-IR system, the uncertainty was reduced from 200 *ppb* to about 100 *ppb*. The results from another five compound measurement with this new setup, show this improvement, especially for toluene.

I noticed that there was significant fluctuation in the laser output power from scan to scan and suspected that a single reference spectrum, taken at the beginning of each experiment, would not be adequate. I therefore installed a second detector into the mid-IR setup to record real-time reference spectra. I also slightly increased the path length from 100 m to 110 m in this new setup. Results from three more five compound measurements using this double detector mid-IR system with 110 m path length, show improvement compared to the previous system especially for ethylbenzene. The uncertainty decreased from 100 *ppb* to 60 *ppb* which is less than one third of uncertainty in the first mid-IR setup with 70 m path length.

Chapter 4

Conclusions and Future Work

This work illustrates the advantages and disadvantages involved in the application of a widely tunable continuous wave external cavity quantum cascade laser system, for the simultaneous detection of BTEX trace gas concentrations during the chemical reactions of these gases with hydroxyl radicals inside a simulation chamber. Mid-IR measurements are based on continuous sampling from the photoreaction chamber into a Herriott multipass cell at room temperature and atmospheric pressure.

The results for benzene are in good agreement with UV DOAS data but in limited agreement for other gases. This encouraged us to go further and improve the mid-IR system to achieve lower detection limits by using longer path lengths and also the two detectors in the mid-IR setup. We have also verified the formation of aerosol particles using a particle counter and a by-product from reactions of BTEX gases with hydroxyl radicals in our simulation chamber. We were only able to detect the by-product peaks using the mid-IR system which highlights the usefulness of mid-IR absorption spectroscopy in gas sensing.

Using EC-QCL in BTEX monitoring is a promising method for future air quality monitoring and volatile organic compound detection, as it gives us real time data over long path lengths without suffering much from beam divergence and also light scattering from particles. This mid-IR system also has least interference from atmospheric components absorption, including carbon dioxide and water.

This type of mid-IR system has the potential to be used as a research tool for longer, open-path measurements and as a component of local or regional atmospheric

trace gas monitoring because of its minimal size, vibration control, and electrical power requirements.

Future improvement of this method includes implementing the multipass cell inside the photoreaction chamber to be able to do in situ mid-IR absorption spectroscopy measurements in order to address problems associated with sampling. Additionally, path length extension will help to improve the sensitivity of this method towards ambient gas concentrations. The final step would be doing longer, open-path measurements to get real atmospheric data.

References

[1] S. Parker, *McGraw-Hill Concise Encyclopedia of Science & Technology*, ser. McGraw-Hill Concise Encyclopedia of Science & Technology. McGraw-Hill, 1984.

[2] D. Rex, *Climate of the Free Atmosphere*, ser. World survey of climatology. Elsevier Pub. Co., 1969, no. v. 4.

[3] U. Platt and J. Stutz, *Differential Optical Absorption Spectroscopy: Principles and Applications*, ser. Physics of Earth and Space Environments. Springer, 2007.

[4] J. de Gouw and C. Warneke, "Measurements of Volatile Organic Compounds in the Earth's Atmosphere using Proton-ransfer-reaction Mass Spectrometry," *Mass Spectrometry Reviews*, vol. 26, no. 2, pp. 223–257, 2007.

[5] A. Guenther, C. N. Hewitt, D. Erickson, R. Fall, C. Geron, T. Graedel, P. Harley, L. Klinger, M. Lerdau, W. McKay, and et al., "A Global Model of Natural Volatile Organic Compound Emissions," *Journal of Geophysical Research*, vol. 100, no. D5, pp. 8873–8892, 1995.

[6] A. Guenther, T. Karl, P. Harley, C. Wiedinmyer, P. I. Palmer, and C. Geron, "Estimates of Global Terrestrial Isoprene Emissions using MEGAN (Model of Emissions of Gases and Aerosols from Nature)," *Atmospheric Chemistry and Physics Discussions*, vol. 6, no. 1, pp. 107–173, 2006.

[7] H. R. Friedli, E. Atlas, V. R. Stroud, L. Giovanni, T. Campos, and L. F. Radke, "Volatile Organic Trace Gases Emitted from North American Wildfires," *Global Biogeochemical Cycles*, vol. 15, pp. 435–452, 2001.

[8] M. O. Andreae and P. Merlet, "Emission of Trace Gases and Aerosols from Biomass Burning," *Global Biogeochemical Cycles*, vol. 15, no. 4, 2001.

[9] M. Lippmann, *Environmental Toxicants: Human Exposures and Their Health Effects.* John Wiley & Sons, 2009.

[10] J. Seinfeld and S. Pandis, *Atmospheric Chemistry and Physics: From Air Pollution to Climate Change*, ser. A Wiley-Intersciencie publications. Wiley, 2006.

[11] C. Young, "FT-IR and Quantum Cascade Laser Spectroscopy towards a Handheld Trace Gas Sensor for Benzene, Toluene, and Xylenes (BTX)," 2009.

[12] *BTEX (Benzene, Toluene, Ethylbenzene, and Xylenes).* The Ohio Department of Health, 2009.

[13] M. T. Parsons, I. Sydoryk, A. Lim, T. J. McIntyre, J. Tulip, W. Jaeger, and K. McDonald, "Real-time monitoring of benzene, toluene, and p-xylene in a photoreaction chamber with a tunable mid-infrared laser and ultraviolet differential optical absorption spectroscopy," *Appl. Opt.*, vol. 50, no. 4, pp. A90–A99, Feb 2011.

[14] C. Song, K. Na, B. Warren, Q. Malloy, and D. R. Cocker, "Secondary Organic Aerosol Formation from m-Xylene in the Absence of NOx," *Environmental Science and Technology*, vol. 41, no. 21, pp. 7409–7416, 2007.

[15] U. Poschl, "Atmospheric Aerosols: Composition, Transformation, Climate and Health Effects," *Angewandte Chemie International Edition*, vol. 44, no. 46, pp. 7520–7540, 2005.

[16] J. G. Calvert, R. Atkinson, K. H. Becker, R. M. Kamens, J. H. Seinfeld, T. J.Wallington, and G. Yarwood, *The Mechanisms of Atmospheric Oxidation of Aromatic Hydrocarbons.* Oxford University Press, New York, NY, 2002.

[17] D. M. Rank, C. H. Townes, and W. J. Welch, "Interstellar Molecules and Dense Clouds," *Science*, vol. 174, no. 4014, pp. 1083–1101, 1971.

[18] R. G. Zepp, B. C. Faust, and J. Hoigne, "Hydroxyl Radical Formation in Aqueous Reactions (pH 3-8) of Iron(II) with Hydrogen Peroxide: the Photo-Fenton

Reaction," *Environmental Science & Technology*, vol. 26, no. 2, pp. 313–319, 1992.

[19] J. Löndahl, E. Swietlicki, E. Lindgren, and S. Loft, "Aerosol Exposure Versus Aerosol Cooling of Climate: What is the Optimal Emission Reduction Strategy for Human Health?" *Atmospheric Chemistry and Physics*, vol. 10, no. 19, pp. 9441–9449, 2010.

[20] NAPCA, *Air Quality Criteria for Particulate Matter.* U.S. Department of Health, Education, and Welfare, Public Health Service, 1969.

[21] K. Wark, C. F. Warner, and W. T. Davis, *Air Pollution: Its Origin and Control, 3rd ed.* Addison-Wesley: Menlo Park, CA, 1998.

[22] B. J. Finlayson-Pitts and J. N. Pitts, *Chemistry of the Upper and Lower Atmosphere: Theory, Experiments and Applications.* Academic Press: San Diego, CA, 2000.

[23] S. and Twomey, "Pollution and the Planetary Albedo," *Atmospheric Environment (1967)*, vol. 8, no. 12, pp. 1251 – 1256, 1974.

[24] V. Carvalho, J. Gabriel Lopes, H. G. Ramos, and F. Correa Alegria, *City-wide Mobile Air Quality Measurement System.* IEEE, 2009, pp. 546–551.

[25] A. J. McMichael, R. E. Woodruff, and S. Hales, "Climate Change and Human Health: Present and Future Risks," *The Lancet*, vol. 367, no. 9513, pp. 859 – 869, 2006.

[26] J. Atienza, P. Aragon, M. A. Herrero, R. Puchades, and A. Maquieira, "State of the Art in the Determination of MTBE in Natural Waters and Soils," *Crit. Rev. Anal. Chem.*, vol. 35, pp. 317–337, 2005.

[27] K.-H. Kim, S. K. Pandey, and R. Pal, "Analytical Bias among Different Gas Chromatographic Approaches using Standard BTX Gases and Exhaust Samples," *Journal of Separation Science*, vol. 32, no. 4, pp. 549–558, 2009.

[28] K. Elke, E. Jermann, J. Begerow, and L. Dunemann, "Determination of Benzene, Toluene, Ethylbenzene and Xylenes in Indoor Air at Environmental Levels

using Diffusive Samplers in Combination with Headspace Solid-phase Microextraction and High-resolution Gas Chromatography-flame Ionization Detection," *Journal of Chromatography A*, vol. 826, no. 2, pp. 191–200, 1998.

[29] P. Kalabokas, J. Hatzianestis, J. Bartzis, and P. Papagiannakopoulos, "Atmospheric Concentrations of Saturated and Aromatic Hydrocarbons around a Greek Oil Refinery," *Atmospheric Environment*, vol. 35, no. 14, pp. 2545 – 2555, 2001.

[30] F. Augusto, J. Koziel, and J. Pawliszyn, "Design and Validation of Portable SPME Devices for Rapid Field Air Sampling and Diffusion-Based Calibration," *Analytical Chemistry*, vol. 73, no. 3, pp. 481–486, 2001.

[31] J. Koziel, M. Jia, and J. Pawliszyn, "Air Sampling with Porous Solid-Phase Microextraction Fibers," *Analytical Chemistry*, vol. 72, no. 21, pp. 5178–5186, 2000, pMID: 11080861.

[32] F. V. Parreira, C. C. R. De, and C. Z. L. De, "Evaluation of Indoor Exposition to Benzene, Toluene, Ethylbenzene, Xylene, and Styrene by Passive Sampling with a Solid-phase Microextraction Device," *Journal of chromatographic science*, vol. 40, no. 3, pp. 122–126, 2002.

[33] F. Santos and M. Galceran, "Modern Developments in Gas Chromatography-Mass Spectrometry-Based Environmental Analysis," *Journal of Chromatography A*, vol. 1000, no. 1-2, pp. 125 – 151, 2003.

[34] H. L. C. Meuzelaar, J. P. Dworzanski, N. S. Arnold, W. H. McClennen, and D. J. Wager, "Advances in Field-Portable Mobile GC/MS Instrumentation," *Field Analytical Chemistry and Technology*, vol. 4, pp. 3–13, 2000.

[35] H. Skov, A. Lindskog, F. Palmgren, and C. S. Christensen, "An Overview of Commonly used Methods for Measuring Benzene in Ambient Air," *Atmospheric Environment*, vol. 35, Supplement 1, no. 0, pp. S141 – S148, 2001.

[36] K. Badjagbo, S. Sauve, and S. Moore, "Real-Time Continuous Monitoring Methods for Airborne VOCs," *TrAC Trends in Analytical Chemistry*, vol. 26, no. 9, pp. 931 – 940, 2007.

[37] S. Zampolli, I. Elmi, J. StÃijrmann, S. Nicoletti, L. Dori, and G. Cardinali, "Selectivity Enhancement of Metal Oxide Gas Sensors using a Micromachined Gas Chromatographic Column," *Sensors and Actuators B: Chemical*, vol. 105, no. 2, pp. 400 – 406, 2005.

[38] S. Zampolli, I. Elmi, F. Mancarella, P. Betti, E. Dalcanale, G. C. Cardinali, and M. Severi, "Real-time monitoring of sub-ppb concentrations of aromatic volatiles with a mems-enabled miniaturized gas-chromatograph," *Sensors and Actuators B: Chemical*, vol. 141, no. 1, pp. 322–328, 2009.

[39] E. Sokol, K. E. Edwards, K. Qian, and R. G. Cooks, "Rapid Hydrocarbon Analysis using a Miniature Rectilinear Ion Trap Mass Spectrometer," *Analyst*, vol. 133, pp. 1064–1071, 2008.

[40] J. M. Plane and A. Saiz-Lopez, *UV-Visible Differential Optical Absorption Spectroscopy (DOAS).* Blackwell Publishing, 2007, pp. 147–188.

[41] R. Volkamer, L. T. Molina, M. J. Molina, T. Shirley, and W. H. Brune, "DOAS Measurement of Glyoxal as an Indicator for Fast VOC Chemistry in Urban Air," *Geophys. Res. Lett.*, vol. 32, 2005.

[42] R. Volkamer, T. Etzkorn, A. Geyer, and U. Platt, "Correction of the Oxygen Interference with UV Spectroscopic (DOAS) Measurements of Monocyclic Aromatic Hydrocarbons in the Atmosphere," *Atmos. Environ.*, vol. 32, 1998.

[43] R. White, *Chromatography/Fourier Transform Infrared Spectroscopy and its Applications*, ser. Practical spectroscopy. M. Dekker, 1990.

[44] W. Lau, *Infrared Characterization for Microelectronics.* World Scientific Pub Co Inc, 1999.

[45] J. Hollas, *Modern Spectroscopy.* Wiley, 2004.

[46] K. Schafer, "Non-Intrusive Measurements of Aircraft and Rocket Exhaust Emissions," *Air Space Europe*, vol. 3, no. 1-2, pp. 104–108, 2001.

[47] J. Faist, F. Capasso, D. L. Sivco, C. Sirtori, A. L. Hutchinson, and A. Y. Cho, "Quantum cascade laser," *Science*, vol. 264, no. 5158, pp. 553–556, 1994.

[48] I. Sydoryk, A. Lim, W. Jaeger, J. Tulip, and M. T. Parsons, "Detection of benzene and toluene gases using a midinfrared continuous-wave external cavity quantum cascade laser at atmospheric pressure," *Appl. Opt.*, vol. 49, 2010.

[49] C. Gmachl, F. Capasso, D. L. Sivco, and A. Y. Cho, "Recent Progress in Quantum Cascade Lasers and Applications," *Rep. Prog. Phys.*, vol. 64, 2001.

[50] A. A. Kosterev and F. K. Tittel, "Chemical sensors based on quantum cascade lasers," *IEEE J. Quantum Electron.*, vol. 38, 2002.

[51] A. Kosterev, F. Tittel, R. Köhler, C. Gmachl, F. Capasso, D. Sivco, A. Cho, S. Wehe, and M. Allen, "Thermoelectrically Cooled Quantum-Cascade-Laser-based Sensor for the Continuous Monitoring of Ambient Atmospheric Carbon Monoxide," *Applied optics*, vol. 41, no. 6, pp. 1169–1173, 2002.

[52] Q. Shi, D. D. Nelson, J. B. McManus, M. S. Zahniser, M. E. Parrish, R. E. Baren, K. H. Shafer, and C. N. Harward, "Quantum Cascade Infrared Laser Spectroscopy for Real-Time Cigarette Smoke Analysis," *Analytical Chemistry*, vol. 75, no. 19, pp. 5180–5190, 2003.

[53] W. H. Weber, J. T. Remillard, R. E. Chase, J. F. Richert, F. Capasso, C. Gmachl, A. L. Hutchinson, D. L. Sivco, J. N. Baillargeon, and A. Y. Cho, "Using a Wavelength-Modulated Quantum Cascade Laser to Measure NO Concentrations in the Parts-per-Billion Range for Vehicle Emissions Certification," *Appl. Spectrosc.*, vol. 56, no. 6, pp. 706–714, Jun 2002.

[54] D. Weidmann, A. A. Kosterev, C. Roller, R. F. Curl, M. P. Fraser, and F. K. Tittel, "Monitoring of Ethylene by a Pulsed Quantum Cascade Laser," *Appl. Opt.*, vol. 43, no. 16, pp. 3329–3334, Jun 2004.

[55] G. P. Luo, C. Peng, H. Q. Le, S. S. Pei, W.-Y. Hwang, B. Ishaug, J. Um, J. N. Baillargeon, and C.-H. Lin, "Grating-Tuned External-Cavity Quantum-Cascade Semiconductor Lasers," *Applied Physics Letters*, vol. 78, no. 19, pp. 2834–2836, 2001.

[56] G. Totschnig, F. Winter, V. Pustogov, J. Faist, and A. Müller, "Mid-Infrared External-Cavity Quantum-Cascade Laser," *Opt. Lett.*, vol. 27, no. 20, pp. 1788–1790, Oct 2002.

[57] G. Luo, C. Peng, H. Le, S.-S. Pei, H. Lee, W.-Y. Hwang, B. Ishaug, and J. Zheng, "Broadly Wavelength-Tunable External Cavity, Mid-Infrared Quantum Cascade Lasers," *Quantum Electronics, IEEE Journal of*, vol. 38, no. 5, pp. 486 –494, may 2002.

[58] R. Maulini, A. Mohan, M. Giovannini, J. Faist, and E. Gini, "External Cavity Quantum-Cascade Laser Tunable from 8.2 to 10.4 mu m using a Gain Element with a Heterogeneous Cascade," *Applied Physics Letters*, vol. 88, no. 20, p. 201113, 2006.

[59] R. Maulini, M. Beck, J. Faist, and E. Gini, "Broadband Tuning of External Cavity Bound-to-Continuum Quantum-Cascade Lasers," *Applied Physics Letters*, vol. 84, no. 10, pp. 1659–1661, 2004.

[60] G. Wysocki, R. Curl, F. Tittel, R. Maulini, J. Bulliard, and J. Faist, "Widely Tunable Mode-Hop Free External Cavity Quantum Cascade Laser for High Resolution Spectroscopic Applications," *Applied Physics B: Lasers and Optics*, vol. 81, pp. 769–777, 2005.

[61] M. Beck, D. Hofstetter, T. Aellen, J. Faist, U. Oesterle, M. Ilegems, E. Gini, and H. Melchior, "Continuous Wave Operation of a Mid-Infrared Semiconductor Laser at Room Temperature," *Science*, vol. 295, 2002.

[62] C. F. Bohren and D. Huffman, *Absorption and scattering of light by small particles*, ser. Wiley science paperback series. Wiley, 1983.

[63] W. Hinds, *Aerosol technology: properties, behavior, and measurement of airborne particles*, ser. Wiley-Interscience. Wiley, 1999.

[64] D. E. Heard, *Analytical Techniques for Atmospheric Measurement.* Oxford: Wiley-Blackwell.

[65] TSI Incorporated, "Condensation Particle Counter Model 3771," 2007.

[66] Ocean Optics, "HR2000+ High-speed Fiber Optic Spectrometer," 2010.

[67] J. B. McManus, P. L. Kebabian, and W. S. Zahniser, "Astigmatic Mirror Multipass Absorption Cells for Longpath Length Spectroscopy," *Appl. Opt.*, vol. 34, 1995.

[68] J. Manne, W. Jaeger, and J. Tulip, "Sensitive Detection of Ammonia and Ethylene with a Pulsed Quantum Cascade Laser using Intra and Interpulse Spectroscopic Techniques," *Applied Physics B: Lasers and Optics*, vol. 94, pp. 337–344, 2009.

[69] J. Houghton, *Physics of Atmospheres*. Cambridge Univ Pr, 2002.

[70] A. McNaught and A. Wilkinson, *IUPAC Compendium of Chemical Terminology*. Blackwell Scientific Publications, 1997, vol. 2.

[71] S. W. Sharpe, T. J. Johnson, R. L. Sams, P. M. Chu, G. C. Rhoderick, and P. A. Johnson, "Gas-Phase Databases for Quantitative Infrared Spectroscopy," *Appl. Spectrosc.*, vol. 58, no. 12, pp. 1452–1461, Dec 2004.

[72] S. Fally, M. Carleer, and A. C. Vandaele, "UV Fourier Transform Absorption Cross Sections of Benzene, Toluene, meta-, ortho-, and para-Xylene," *Journal of Quantitative Spectroscopy and Radiative Transfer*, vol. 110, no. 9-10, pp. 766 – 782, 2009.

[73] J. Ripp and W. L. C. . R. Program, *Analytical detection limit guidance & laboratory guide for determining method detection limits*, ser. Analytical Detection Limit Guidance & Laboratory Guide for Determining Method Detection Limits. Wisconsin Dept. of Natural Resources, Laboratory Certification Program, 1996.

[74] D. Skoog and D. West, *Principles of Instrumental Analysis*. Saunders College Publishing New York, 1985, vol. 4.

[75] S. Bell, "A beginner's guide to uncertainty in measurement," *Measurement Good Practice Guide*, no. 11, 2001.

[76] D. C. Harris, *Quantitative Chemical Analysis*. W.H. Freeman, 1999.

[77] C. Gmachl, D. L. Sivco, R. Colombelli, F. Capasso, and A. Y. Cho, "Ultra-broadband semiconductor laser," *Nature*, vol. 415, 2002.

Appendices

Appendix A

Conference Paper

The submitted abstract to the 2012 OSA Optics & Photonics Congress can be found in this part.

Monitoring Multiple Trace Gas Species during Secondary Organic Aerosol Formation in a Smog Simulation Chamber using Mid-IR Laser and UV Spectroscopic Methods

Boshra Momen Nejad,* Matthew T. Parsons, Ihor Sydoryk, Elijah Schnitzler, Alan Lim, John Tulip, Wolfgang Jaeger, and Karen McDonald

University of Alberta, Concordia University College of Alberta

**Corresponding author: momennej@ualberta.ca*

Abstract: We demonstrate our progress in developing an application of mid-IR External Cavity Quantum Cascade Laser (EC-QCL) absorption spectroscopy for concentration measurements of benzene, toluene, ethylbenzene and o- and p-xylene (i.e., BTEX) in a simulation chamber.

OCIS codes: (300.6340) Spectroscopy, infrared; (140.5965) Semiconductor lasers, quantum cascade

1. Introduction

BTEX gases (Benzene, Toluene, ethylbenzene, o-, and p-xylene) mostly produced by petroleum industries, are toxic and affect human health and the Earth's environment [9]. They have also been shown to produce other air pollutants such as aerosol particles via photochemical reactions [13], [14] with hydroxyl radicals when exposed to UV radiation.

Modern improvements in quantum cascade laser (QCL) technology have opened a new era in spectroscopic measurements of atmospheric gases. Because of their wide range of applicable frequencies, QCLs have been used in many gas-sensing applications that usually require narrow laser line-width and broadly tuned output [49], [50]. A variety of grating-tuned mid infrared external cavity quantum cascade lasers (EC-QCL) with the tunability range of 100 cm^{-1} or even ultra broadband tunable over 750 cm^{-1} have been reported [56]–[59], [77]

In this work, we investigate the applicability of EC-QCL absorption spectroscopy in multi component systems with an interest in interference in measurements from each species. Specifically, we consider multi component systems with benzene, ethylbenzene, toluene, and o- and p-xylenes (BTEX gases). As described before [13], [48] we carried out real time monitoring of the concentration of BTEX trace gas species via mid-IR absorption spectroscopy using an external cavity quantum cascade laser (EC-QCL), tunable in the range of 9.41-9.88 μm (1012-1063 cm^{-1}) during reactions with hydroxyl radicals in a photoreaction chamber. We compare our mid-IR results with UV differential optical absorption spectroscopic measurements, an alternative method for measuring BTEX gas concentrations [40]–[42].

2. Experimental Methods

The smog simulation chamber used in this study is a cube constructed of 0.127 mm thick perfluoroalkoxy (PFA) film with a volume of 1.8 m^3 (Ingeniven Fluoropolymer Solutions). The chamber is irradiated with UV light by an array of 24 fluorescent 32 W black lights with peak emission at 350 nm. Tests were run dynamically with clean, dry air diluting the contents of the simulation chamber while continuously sampling from the chamber. Results are corrected for dilution effects.

Reagent gases (H_2O_2, benzene, toluene, ethylbenzene, o- and p-xylene) were introduced to the smog simulation chamber via liquid injections using a microlitre syringe or flow of clean, dry air through a liquid bubbler.

The mid-IR system has been described in detail previously [13], [48]. The light source for these measurements was a room temperature continuous wave external cavity quantum cascade laser (EC-QCL), tunable between 9.41-9.88 μm with mode hop free tunability from 9.68 - 9.88 μm (1012-1032 cm^{-1}) (Daylight Solutions,

TLS-CW-MHF). Liquid nitrogen cooled mercury-cadmium-telluride (MCT) detectors (Kolmar Technologies, KMPV11) were used for measurements. All mid-IR tests discussed here used an astigmatic Herriott multi-pass cell [67] at atmospheric pressure with two configurations of the multi-pass cell, one with 70 m path length and one with 110 m mounted into an aluminum chamber with a volume of approximately 14.2 L.

The light source for UV differential optical absorption spectroscopy measurements was a broadband deuterium lamp with emission output from 215-400 nm (Ocean Optics, D-2000-S). A grating-based spectrometer was used for these measurements (Ocean Optics, HR-2000+). UV tests were made in situ with a single-pass through the simulation chamber over a path length of 1.2 m [13]. All UV absorption spectra were referenced to filtered, dry air at the start of each test. The mid-IR and UV absorption spectra were transformed to differential optical absorption spectra as described in [13].

3. Results and Discussion

We have measured decreasing BTEX gas concentrations during photochemical reactions with both IR and UV systems. Fig. A.1 (a) shows an example of mid-IR and UV DOAS data obtained during chemical transformation of a mixture of benzene + toluene + ethylbenzene + o-xylene + p-xylene in the photoreaction chamber as a function of time with hydroxyl radicals. Mid-IR data are shown as filled black circles with thick black curves as their fits; UV data are shown as hollow gray circles with thick gray curves as their fits. All data were corrected to account for dilution of the photoreaction chamber content over the course of the reaction. The initial concentration of benzene, toluene, ethylbenzene, o- , and p-xylene measured in IR system was 2.46, 2.66, 2.94, 4.04, 4.23 ppm, respectively. Fig. A.1 (a) shows the measured gas concentrations as a percentage of the original concentration of each gas after corrections for dilution of the photoreaction chamber content. There is a good agreement between measurements of benzene concentrations from the mid-IR and UV systems. For the toluene, ethylbenzene and also o-, and p-xylene concentration measurements, there are some discrepancies between UV and mid-IR results due to interference between toluene and ethylbenzene peaks at approximately 1032

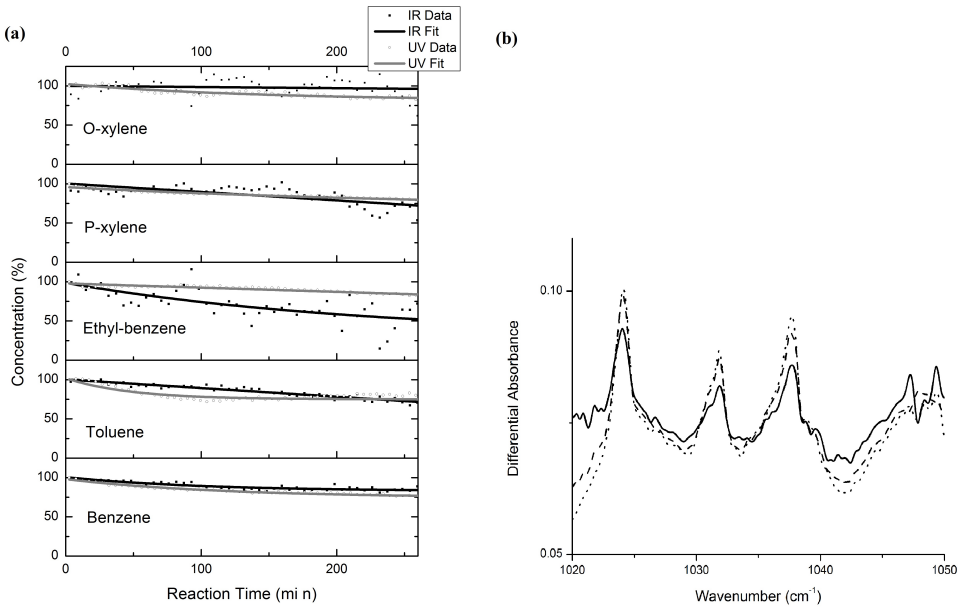

Fig. A.1. (a) Benzene, toluene, ethylbenzene, o- and p-xylene gas concentration measurements in the photoreaction chamber as a function of time. (b) Mid-IR differential optical absorption spectra at specific time intervals for benzene, toluene, ethylbenzene, o- and p-xylene.

cm^{-1} and o-, and p-xylene peaks at approximately 1024 cm^{-1}. Additionally, ethylbenzene and p-xylene exhibit minimal absorption features in the mid-IR range of this particular EC-QCL, which results in increased uncertainty in measuring their concentrations with the EC-QCL used in this study.

In addition to secondary organic aerosol particle formation, we also observed formation of a by-product in the reactions of hydroxyl radicals with BTEX compounds. Fig. A.1 (b) shows an example of mid-IR DOAS spectra for BTEX reactions at 0, 1, and 5 hours of the reactions. Dotted spectra are at t = 0 h, dashed spectra are at t = 1 h (without dilution correction), and solid spectra are at t = 5 h (without dilution correction). Reaction by-product peaks are observed at about 1047 cm^{-1} and 1049 cm^{-1}. Our attempts to elucidate the source of this absorption feature have been unsuccessful (for either organic or inorganic compounds) and we simply label this feature as that of a by- product of the reactions.

No corresponding absorption features from by-products were observed in the UV DOAS spectra during these tests. Therefore, we emphasize the importance of using multiple monitoring methods such as mid-IR and UV DOAS in measuring trace gas concentrations, either in the atmosphere or in simulated environments similar to the

current study.

4. Conclusion

Our efforts in this work illustrate the advantages and disadvantages involved in monitoring the concentrations of multiple BTEX trace gas species in real-time during their chemical transformation in a photoreaction chamber, using a mid-IR tunable EC-QCL. The results from our IR system show formation of unknown by-products while BTEX gases undergo chemical reactions in the chamber. We have noticed that we are only able to detect these peaks in mid-IR region which highlights the use of mid-IR absorption spectroscopy in gas sensing.

5. Acknowledgement

This work was supported by the Natural Sciences and Engineering Research Council of Canada, the National Research Council of Canada (NRC), and the Development Bank of Canada.